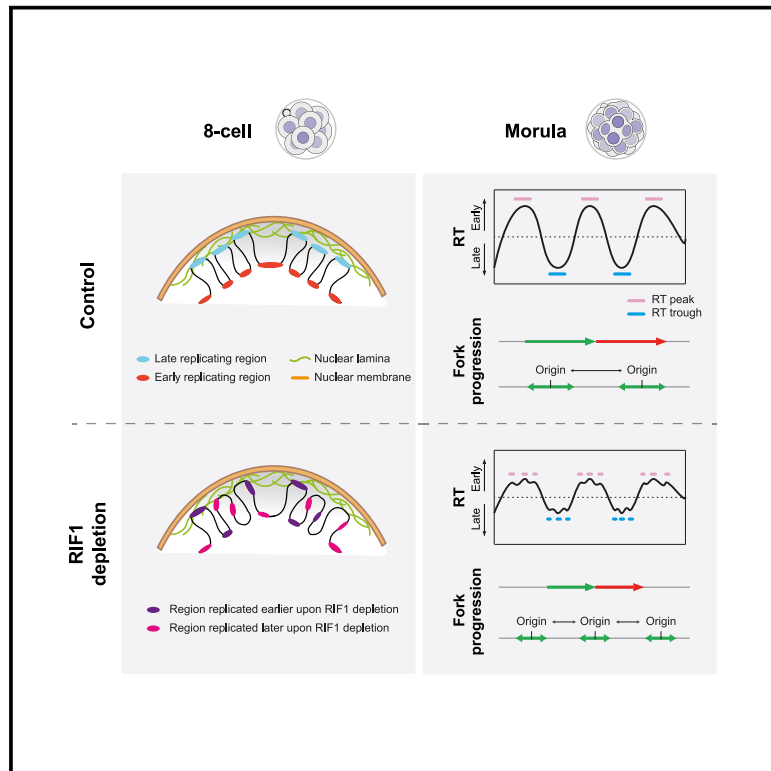


Developmental Cell

RIF1 controls replication timing in early mouse embryos independently of lamina-associated nuclear organization

Graphical abstract



Authors

Tsunetoshi Nakatani, Tamas Schauer, Mrinmoy Pal, ..., Julia Zorn, David M. Gilbert, Maria-Elena Torres-Padilla

Correspondence

torres-padilla@helmholtz-muenchen.de

In brief

Nakatani et al. demonstrate a role for RIF1 in regulating replication timing during mouse embryogenesis. Depletion of RIF1 results in changes in replication timing and in nuclear organization of lamina association, but the changes in RT and lamina association are unrelated.

Highlights

- RIF1 regulates the consolidation of replication timing (RT) during embryogenesis
- RIF1 depletion slows replication fork progression and reduces inter-origin distance
- Depletion of RIF1 results in LADs and iLADs remodeling
- Changes in LAD/iLAD and RT upon RIF1 depletion do not show a consistent relationship

Short article

RIF1 controls replication timing in early mouse embryos independently of lamina-associated nuclear organization

Tsunetoshi Nakatani,¹ Tamas Schauer,¹ Mrinmoy Pal,¹ Andreas Ettinger,¹ Luis Altamirano-Pacheco,¹ Julia Zorn,² David M. Gilbert,³ and Maria-Elena Torres-Padilla^{1,4,5,*}

¹Institute of Epigenetics and Stem Cells (IES), Helmholtz Zentrum München, 81377 München, Germany

²Core Facility Laboratory Animal Services, Helmholtz Zentrum München, 81377 München, Germany

³Laboratory of Chromosome Replication and Epigenome Regulation, San Diego Biomedical Research Institute, San Diego, CA 92121, USA

⁴Faculty of Biology, Ludwig-Maximilians Universität, München, Germany

⁵Lead contact

*Correspondence: torres-padilla@helmholtz-muenchen.de

<https://doi.org/10.1016/j.devcel.2025.03.016>

SUMMARY

Cells must duplicate their genome before they divide to ensure equal transmission of genetic information. The genome is replicated with a defined temporal order, replication timing (RT), which is cell-type specific and linked to 3D-genome organization. During mammalian development, RT is initially not well defined and becomes progressively consolidated from the 4-cell stage. However, the molecular regulators are unknown. Here, by combining loss-of-function analysis with genome-wide investigation of RT in mouse embryos, we identify Rap1 interacting factor 1 (RIF1) as a regulator of the progressive consolidation of RT. Embryos without RIF1 show DNA replication features of an early, more totipotent state. RIF1 regulates the progressive stratification of RT values and its depletion leads to global RT changes and a more heterogeneous RT program. Developmental RT changes are disentangled from changes in transcription and nuclear organization, specifically nuclear lamina association. Our work provides molecular understanding of replication and genome organization at the beginning of mammalian development.

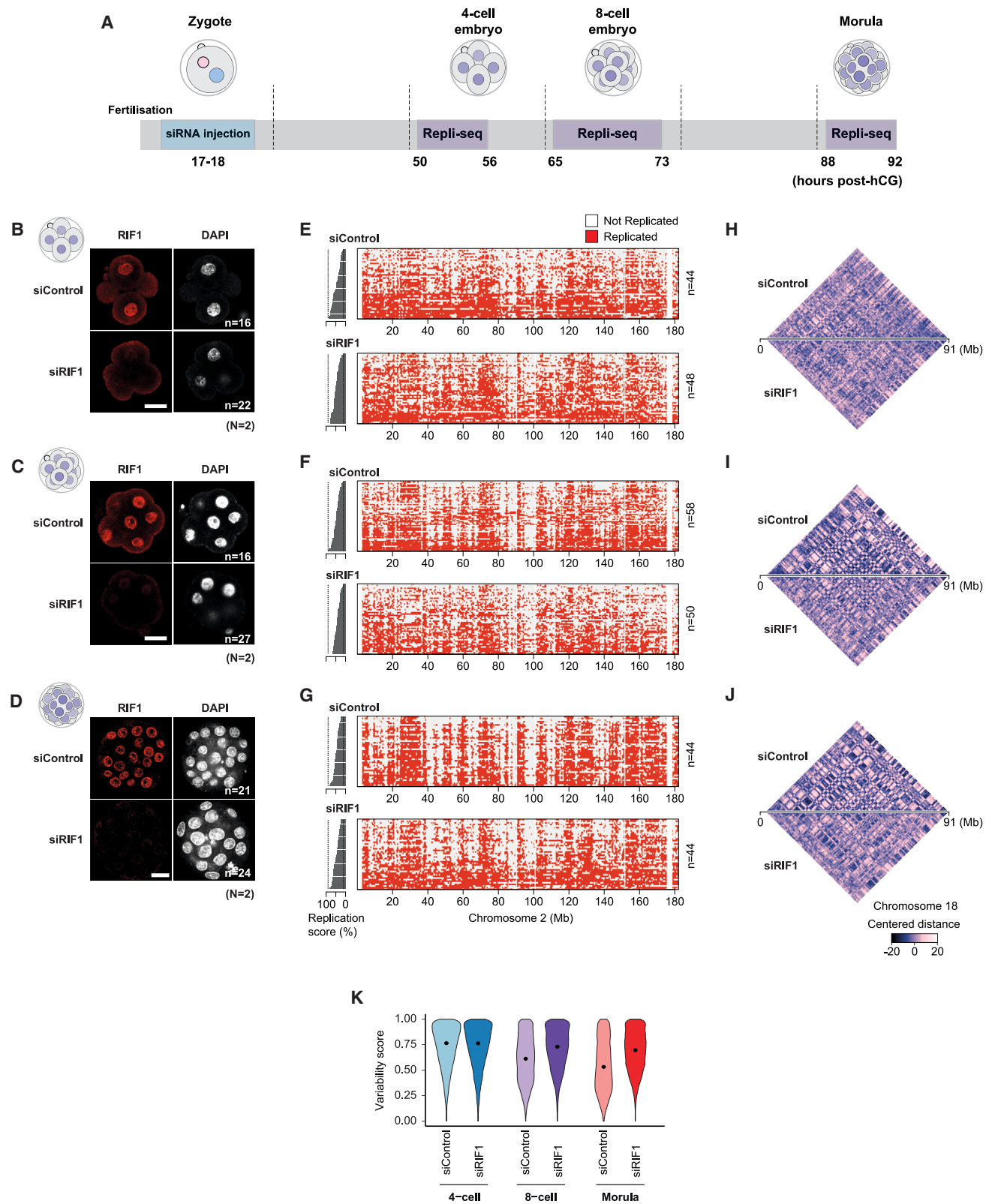
INTRODUCTION

Genome duplication before cell division is fundamental for transmitting genetic information. DNA replication occurs in a temporally coordinated manner, referred to as replication timing (RT),^{1,2} whereby specific genomic regions replicate at specific times during S phase. RT is linked to chromatin restoration during S phase, presumably because chromatin modifier complexes associated with the replisome during early and late S phase differ.^{3,4} For example, histone H3K4me3 methyltransferases are more abundant in replicated chromatin from early-replicating regions.³ Accordingly, genomic regions replicating earlier are typically euchromatic, whereas heterochromatin tends to replicate late in S phase.^{5,6}

RT is thought to be established in G1 of the cell cycle⁷ and is executed through replication initiation at specific regions (initiation zones [IZs]), where replication origins are activated in a coordinated fashion.^{8,9} RT is an epigenetic fingerprint, is cell-type specific² and is associated with the restoration of chromatin states^{3,4} during replication. Thus, understanding the molecular regulation of RT is fundamental for understanding the faithful transmission and re-establishment of chromatin states. During embryonic development in mammals, RT is initially not well

defined in zygotes and 2-cell stage embryos but becomes progressively defined as development proceeds, from the 4-cell stage onward.¹⁰ In mouse embryonic stem cells (ESCs), replication domains also consolidate upon differentiation, primarily by fusing into larger domains.⁵ In mouse embryos, the emergence of the RT program involves a progressive decrease in heterogeneity and the fusion into larger IZs and is accompanied by the segregation into well-partitioned early and late RT values throughout S phase.^{10,11}

The mechanisms regulating RT are largely unknown but are likely to occur by regulating the local probability of initiation. Among the factors regulating origin firing, Rap1 interacting factor 1 (RIF1) suppresses firing of late replication origins¹² and is known to ensure early replication of highly transcribed genes.¹³ RIF1 is dispensable for mouse and human ESC self-renewal.^{14,15} However, RIF depletion in human ESCs leads to a complete erasure of the RT program and downstream effects on histone modifications and 3D genome organization, demonstrating that RT acts upstream of the epigenetic make-up of human cells.¹⁵ In mouse ESCs, RIF1 loss also leads to altered RT, activation of DNA replication checkpoint response, and decreased cell viability without arresting proliferation.¹⁶ In mice, female RIF1-null embryos die irrespective of the genetic background, but



(legend on next page)

male RIF1 null embryos survive, albeit at reduced frequencies depending on genetic background.^{17–20}

In zebrafish, RIF1 is dispensable for development, but zygotic depletion of RIF1 impairs female sex determination.²¹ RT has been mapped during early development in zebrafish, where a defined temporal RT order is detected already in pre-mid-blastula-transition stage embryos, prior to zygotic genome activation (ZGA).²² This contrasts with the mouse, in which RT is not yet fully defined at the time of ZGA.¹⁰ Whole-genome RT analyses conducted before and after zygotic transcription in zebrafish indicated that RIF1 “sharpens” RT profiles genome-wide.²¹ In mice, RIF1 is deposited as maternal protein²³ and is present as several isoforms of different lengths, which have been documented using different antibodies.¹⁴ However, whether RIF1 plays a role *in vivo* at the earliest developmental stages after fertilization in mammals has not been addressed.

The separation into early and late replication domains is associated with 3D genome organization, with late-replicating domains generally corresponding to B compartments and lamina-associated domains (or LADs)^{2,24} and early-replicating domains corresponding to A compartments and inter-LADs (iLADs).^{25,26} The control of RT and 3D genome organization may obey independent and convergent mechanisms and is currently an area of intense research.²⁷ In mouse embryos, the relationship between RT and LADs emerges at different developmental times. LADs are established immediately after fertilization, potentially priming early- and late-replicating domains.²⁸ By contrast, A and B compartments, although detectable in zygotes, undergo developmental maturation by progressive increase in compartment strength,^{29,30} and partitioning of early and late RT during development coincides with the maturation of A and B compartments.¹⁰ While there is a clear structural correlation between these three pillars of nuclear organization, they can be molecularly disentangled during development. For example, while RT is only mildly affected upon transcriptional inhibition at ZGA,¹⁰ LADs are severely remodeled in the absence of transcription, and embryonic LADs at the 2-cell stage are fully dependent on transcriptional activity.³¹ Thus, the molecular dependencies between genome organization and RT and their regulators remain unclear.

Despite the importance of RT for epigenome maintenance, the molecular regulators of RT during development *in vivo* are unknown. Here, we report that RIF1 regulates RT in mouse embryos. Depletion of RIF1 leads to global RT changes that are characteristic of a more immature, less defined RT program. These changes are accompanied by an increase in the heterogeneity of the RT program and a reduction in replication fork speed, also characteristic of earlier developmental stages,³² indicating

that RIF1 orchestrates DNA replication at different levels. By addressing RIF1 function at three developmental times, we demonstrate that RIF1 regulates RT independently of changes in gene expression and lamina association. Our work identifies a key regulator of the developmental consolidation of RT during the establishment of the epigenome at the beginning of development and provides evidence for a non-interdependence of the layers of genome organization.

RESULTS

RIF1 depletion in mouse embryos results in a less coordinated RT program

We recently reported that the RT program is progressively consolidated during pre-implantation development,¹⁰ aligning with the gradual increase in compartment strength.^{29,30} To gain molecular understanding on RT establishment, we asked whether proteins known to regulate RT in other systems are involved in this process. A strong candidate is RIF1 because RIF1 can regulate RT in human and mouse ESCs and regulates RT of heterochromatin after ZGA in *Drosophila*.^{15,16,33–35} In addition, RIF1 regulates RT maturation in zebrafish.²¹

RIF1 is present as a maternally inherited cytoplasmic protein in mouse zygotes and is expressed throughout pre-implantation development.^{14,23} To address whether RIF1 orchestrates RT establishment, we performed RIF1 loss-of-function experiments and examined RT at three different times during development. We aimed to deplete RIF1 from the 4-cell stage, the time at which RT starts to consolidate in mouse embryos,¹⁰ which also coincides with the detection of RIF1 isoforms in the nucleus.¹⁴ We performed small interfering RNA (siRNA) for RIF1 in zygotes and generated single-cell Repli-seq (scRepli-seq) at the 4-cell, 8-cell, and morula stages (Figure 1A). We sequenced a total of 416 single cells (Table S1). We confirmed that RIF1 protein was depleted from the 4-cell stage onward and until the blastocyst stage by performing immunostaining using an antibody recognizing the nuclear RIF1 isoforms (Figures 1B–1D and S1A–S1D).¹⁴ This antibody is expected to recognize full length and some other RIF1 isoforms that are not full length as well.¹⁴ Depletion of RIF1 did not affect developmental progression to the blastocyst stage (Figure S1E), and we did not observe overt morphological abnormalities in these embryos. However, we noted an increase in chromosome imbalance as development proceeds to later developmental stages as determined by the coefficient of variation for the average sequencing read coverage per chromosome (Figure S1F), suggesting a potential effect on genome stability upon RIF1 depletion. To address this and considering that RIF1 plays a role in DNA damage

Figure 1. RIF1 regulates genome-wide RT in mouse embryos

(A) Experimental timeline.

(B–D) RIF1 immunostaining after microinjection in control and RIF1-depleted embryos. *n*: number of embryos analyzed. *N*: number of independent experiments. Scale bar, 25 μ m. Maximum-intensity projections are shown for 8-cell and morula-stage embryos. Four-cell stage embryos were 3D mounted; hence, the cytoplasmic background is higher than in 8-cell and morula stages.

(E–G) Heatmaps of single cells indicating replication status ranked by their percentage of replicated genome (replication score), plotted on the left. Gray: not replicated; red: replicated.

(H–J) Pairwise Manhattan distance between genomic bins on the binary data over a representative chromosome. Distance values are mean-centered, and thus the relative distances are comparable between samples. Darker color indicates higher similarity.

(K) Variability score after RIF1 depletion. Score is 1 when 50% of cells replicated the genomic bin and 0 when either all (100%) or none (0%). Violins show the distribution of scores for all genomic bins. Dots, median.

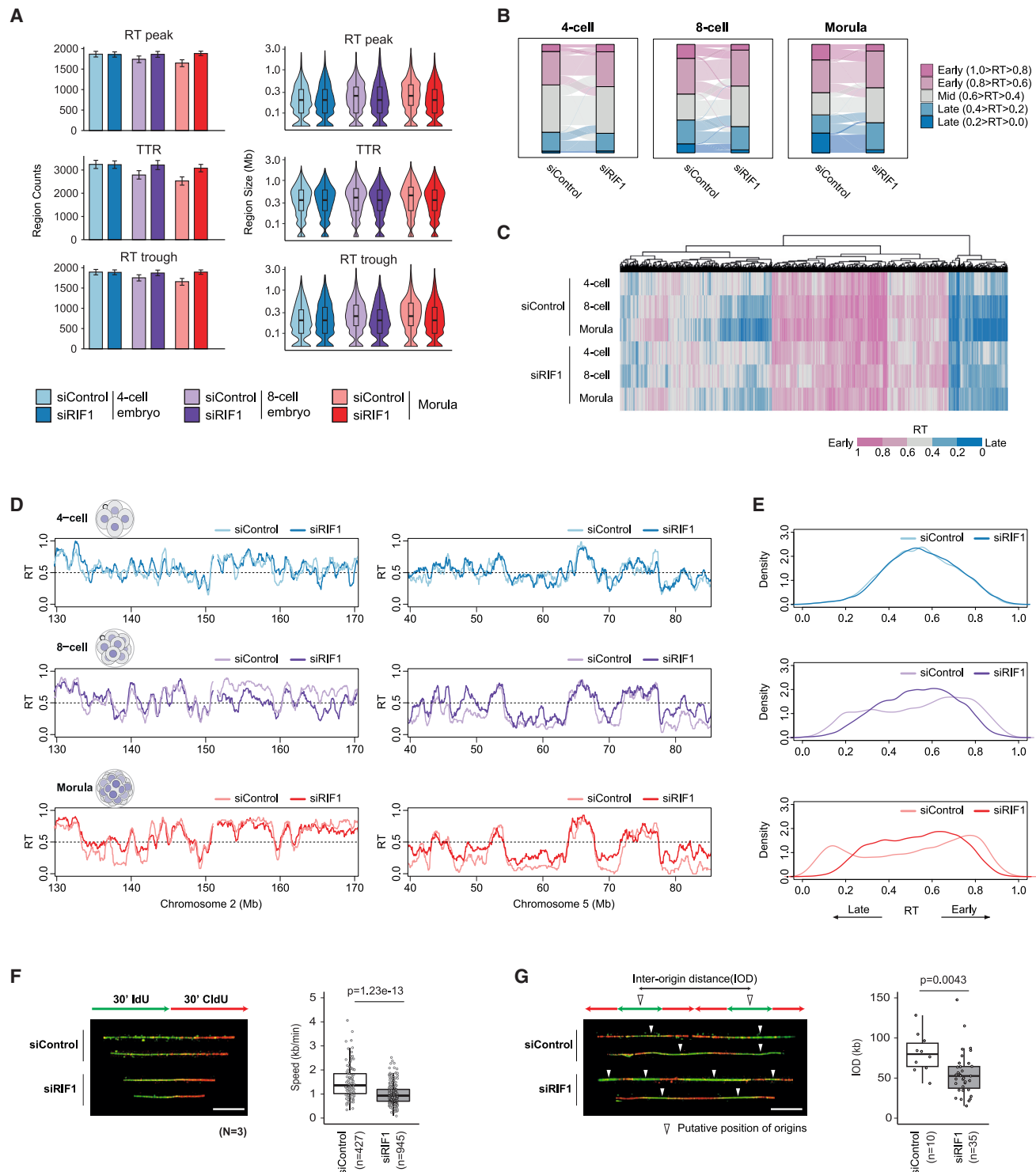


Figure 2. Depletion of RIF1 prevents consolidation of RT during the progression of embryogenesis

(A) Number and size of RT peaks (initiation zones [IZs]); timing transition regions (TTRs); RT troughs (termination zones [TZs]). Error bars in bar plots indicate a 95% bootstrap confidence interval. Statistical analysis in [Figures S2A](#) and [S2B](#). Boxplots inside violin plots show the median and interquartile range (IQR), and whiskers depict the smallest and largest values within $1.5 \times$ IQR.

(B) Alluvial plot depicting RT changes of all genomic bins showing changes of RT after RIF1 depletion. RT values were categorized in 5 groups from earliest ($1.0 > RT > 0.8$) to latest ($0.2 > RT > 0.0$).

(C) Heatmap of RT in RIF1-depleted and control embryos.

(legend continued on next page)

response, we quantified phosphorylation of H2A.X (γ H2A.X) at the morula stage, a proxy for checkpoint activation and DNA damage response downstream of ataxia telangiectasia and Rad3-related (ATR) activity.³⁶ γ H2A.X levels did not increase—and in fact decreased—upon RIF1 depletion (Figure S1G), suggesting no detectable DNA damage nor activation of the DNA damage response in embryos without RIF1. RIF1 depletion did not alter the total number of cells per embryo at the blastocyst stage (Figure S1H), indicating no effect on cellular proliferation. Instead, we noted an increase in the number of cells in mitosis per embryo, suggesting that while RIF1 depletion does not majorly affect cellular proliferation per se, its absence may lead to a prolonged mitosis. This is in line with previous observations in RIF1-depleted human cells, which show an accumulation of cells with a G2/M DNA content.^{15,37}

We generated RT profiles in 4-cell, 8-cell, and morula-stage embryos depleted of RIF1, compared with siRNA controls at the corresponding developmental stage. Sorting cells by their extent of genome replication (replication score) revealed progression through the S phase in RIF1-depleted embryos, with the typical early and late replication patterns (Figures 1E–1G). A visual inspection of RT profiles suggests that RT was globally maintained in embryos despite RIF1 depletion (Figures 1E–1G). However, this analysis also indicated a less defined, fuzzier replication pattern across cells and throughout the genome in RIF1-depleted embryos, particularly at the 8-cell and morula stages (Figures 1E–1G). This suggests a less coordinated RT program upon RIF1 depletion after the 4-cell stage. To address this quantitatively, we computed a matrix with Manhattan distances across cells between all pairs of genomic bins based on the binarized, replicated/unreplicated data. Lower Manhattan distances indicate more similar bins overall, and higher distances indicate more dissimilar bins and, therefore, a less coordinated RT program. In line with previous work, we observe a higher coordination as development proceeds from the 4-cell stage to the morula in controls (Figures 1H–1J). This analysis also indicates that the coordination of the RT program decreases upon RIF1 depletion at all 3 stages analyzed (Figures 1H–1J). Comparing developmental stages suggests that, while the coordination of the RT program also increases in the absence of RIF1, it does so to a lesser extent than in the corresponding controls (Figures 1H–1J). We computed the variability score, which measures the variance of the replication program across cells for each genomic bin.¹⁰ This confirmed that the variability of the RT program decreases progressively from the 4-cell stage and further confirmed that RIF1 depletion increases the variability score at the 8-cell and morula stages (Figure 1K). Statistical analysis using bootstrap (1,000 iterations) indicated that the average variability score is similar between controls and RIF1-depleted embryos at the 4-cell stage but increases significantly upon RIF1 depletion at the 8-cell and morula stages (Figure S1I). These results establish that RIF1 is required for the progressive acquisition

of the coordinated RT program that normally occurs during development from the 4-cell stage. We conclude that RIF1 depletion results in a more variable, less defined RT program in pre-implantation embryos, suggesting that RIF1 mediates the consolidation of the embryonic RT program.

RIF1 regulates the consolidation of RT in mouse embryos

The above data prompted us to address whether RIF1 mediates the developmental consolidation of the RT program. To address this, we examined replication features of RIF1-depleted embryos. In particular, since the developmental consolidation of RT occurs primarily at the level of RT peaks (also known as LZs) and timing transition regions (TTRs),¹⁰ we extracted these features from our scRepli-seq datasets.^{8,10} We also analyzed RT troughs (also known as termination zones), which are regions in which replication forks converge.³⁸ Control embryos showed the expected consolidation trend as development proceeds, with a reduction of the number of RT peaks, RT troughs, and TTRs overall (Figure 2A).¹⁰ The number of RT peaks, TTRs, and RT troughs was unaffected upon RIF1 depletion at the 4-cell stage (Figure 2A). However, the number of all three features was higher in RIF1-depleted 8-cell and morula-stage embryos compared with controls (Figure 2A). Bootstrapping (1,000 iterations) and calculation of confidence intervals¹⁰ indicated that the number and size of RT features were significantly different between controls and RIF1-depleted 8-cell and morula embryos but not in 4-cell stage embryos (Figures S2A and S2B). Thus, the consolidation of RT features past the 4-cell stage is prevented upon RIF1 depletion. This was accompanied by a consequent reduction in the size of RT peaks, TTRs, and RT troughs compared with controls (Figure 2A), pointing toward a more fragmented RT program in RIF1's absence, in line with our interpretation of a less consolidated program upon RIF1 depletion.

We next asked whether RIF1 regulates the order in which the genome replicates during S phase. For this, we investigated the genome distribution into early and late replication. Globally, the RT patterns were maintained across all genomic bins in RIF1-depleted embryos at all stages analyzed (Figure S2C). However, while genome-wide correlations of RT values did not differ much between controls and RIF1-depleted embryos, the skewed distribution of the RT values along the diagonal suggests a deviation of RT between control and RIF1-depleted embryos, particularly at the 8-cell and morula stages (Figure S2C). Indeed, genomic regions replicating early shift to later replication, and late-replicating regions replicate earlier upon RIF1 depletion (Figure S2D). To further investigate this, we stratified the genome into RT values from earliest (RT > 0.8) to latest (RT < 0.2) with increments of 0.2. We first reanalyzed previous data from non-manipulated embryos, which indicate a progressive partitioning into more extreme RT values across the complete S phase (Figure S2E).¹⁰ Our siRNA controls reproduced previous findings

(D) Average RT profiles of RIF1-depleted embryos on representative segments of chromosomes 2 and 5 overlaid with their controls.

(E) Density plots of distribution of RT of 50 kb genomic bins in RIF1-depleted 4-cell, 8-cell, and morula stages overlaid with their controls. Statistical analysis in Figure S2F.

(F and G) DNA-fiber analysis in morula. Fork speed (F), inter-origin distance (IOD) (G), and representative images are shown. Boxplots show the median and IQR, and whiskers depict the smallest and largest values within $1.5 \times$ IQR. Statistical analysis, two-sided Wilcoxon's rank-sum test. Scale bar, 15 μ m. In (F) and (G), n : number of fibers analyzed; N : number of independent experiments.

showing that while most of the genome at the 4-cell stage (44%) shows intermediate RT values ($0.6 > RT > 0.4$), the genome partitions into values spreading the complete S phase progressively thereafter (24% and 21% of the genome in 8-cell and morula-stage displays RT values greater than 0.4 and less than 0.6, respectively) (Figure 2B). By contrast, the same analysis in RIF1-depleted embryos indicated that the distribution of the genome across the S phase in 8-cell and morula embryos resembled that of 4-cell embryos instead of its corresponding 8-cell control (Figure 2B). A detailed analysis of RT values of all genomic regions indicated that while overall early-replicating regions remain so in all conditions, they shift toward earlier RT in control 8-cell stage embryos but not in 8-cell embryos depleted for RIF1 (Figure 2C). This suggests that RIF1 depletion interrupts the natural developmental shift to earlier replication of those regions. We observed a similar pattern in morula-stage embryos (Figure 2C). Likewise, “mid” S phase replicating regions shift to later replication in control 8-cell embryos but not in embryos without RIF1 (Figure 2C). Examining genome-wide RT profiles revealed indeed that RT values tend to move toward mid-values, with some regions that replicate early in controls shifting to later and regions that replicate late shifting to earlier in the absence of RIF1 (Figure 2D). In fact, overlaying the genome-wide distribution of RT values indicated that while control 8-cell and morula RT values separate toward earlier and later RT values, RIF1-depleted embryos do not (Figure 2E). These differences were statistically significant (Figure S2F). Instead, their distribution resembles that of 4-cell stage embryos (Figure 2E). We also calculated the M -value, which is a measure of the replication score at which half of the cells replicate a particular genomic bin.¹⁰ The distribution of the M -values reflects the partitioning of the RT values across the genome. M -values of ESCs and differentiated cells depict a bimodal distribution, indicating a well-spread partitioning of the genome into early versus late RT.^{8,10} By contrast, mouse embryos before the 4-cell stage show a unimodal distribution.¹⁰ In agreement, siControl and siRIF1 embryos showed a similar, largely unimodal distribution at the 4-cell stage (Figure S2G). In the absence of RIF1, 8-cell and morula-stage embryos displayed a spread of M -values (interquartile range [IQR]) similar to control 4-cell stage embryos but differed from control 8-cell and morula embryos (Figures S2G and S2H). This indicates that RIF1 regulates the progressive segregation of the genome into early- and late-replicating domains during development *in vivo*.

Lastly, we computed the T_{width} , which reflects RT heterogeneity across cells.³⁸ Depletion of RIF1 significantly increases T_{width} compared with controls at the 8-cell and morula stages but not at the 4-cell stage (Figures S2I and S2J). Thus, RIF1 depletion alters RT heterogeneity, suggesting that RIF1 contributes to the robustness of the emerging embryonic replication program by limiting cell-to-cell variability. Notably, in all the above analyses, the replication features of RIF1-depleted embryos resembled those of control embryos at earlier stages. Overall, the above data suggest that RIF1 depletion results in an immature RT program.

We then asked whether the more immature RT program upon RIF1 depletion involves molecular properties of the DNA replication process itself, for example, replication fork dynamics. To address this, we performed DNA-fiber analyses to measure

replication fork speed. In normal development, replication fork speed is initially slow and increases as development proceeds.^{32,39} Remarkably, RIF1 depletion leads to a slower replication fork speed (Figure 2F), with morula embryos depleted of RIF1 replicating with a similar fork speed as control 8-cell stage embryos.³² This is accompanied by a reduction in the inter-origin distance (Figure 2G). These observations suggest that RIF1-depleted embryos fire more origins, which characterizes the earliest stages of development,³² and supports our interpretations of a more immature DNA replication program upon RIF1 depletion. We conclude that RIF1 depletion slows the replication fork, resulting in features of the replication fork characteristic of earlier developmental stages. This also suggests that the developmental acquisition of an orderly RT program and the increase in replication fork speed during pre-implantation development may be functionally related.

RIF1 establishes developmental patterns of RT

Considering the temporal, developmental-specific phenotypes upon RIF1 depletion, we next investigated whether RIF1 regulation of RT is stage specific. We asked whether changes in RT are inherited to the next developmental stage or whether RT changes elicited upon RIF1 depletion are specific to each developmental stage. To reveal potential developmental patterns, we first performed a principal-component analysis (PCA) of RT values from all control (siControl) and RIF1-depleted (siRIF1) embryos together with wild-type embryos from zygote to morula stage.¹⁰ As expected, zygotes and 2-cell stage clustered away from all other later stages (Figure 3A). In addition, while control embryos clustered with their respective non-manipulated stage, RIF1-depleted embryos consistently clustered with earlier developmental stages (Figure 3A). Namely, 8-cell RIF1-depleted embryos clustered together with 4-cell stage embryos, and morula RIF1-depleted embryos clustered closer to 8-cell controls than to morula controls (Figure 3A). Overall, this suggests that RIF1 may function to set developmentally specific RT changes that, upon depletion, are not properly established. Interestingly, all 4-cell stage embryos clustered largely together, whether controls or RIF1-depleted (Figure 3A). This suggests that the function of RIF1 in establishing stage-specific developmental RT programs occurs concomitantly with the consolidation of the RT program, which is known to take place from the 4-cell stage.¹⁰

To further examine a role of RIF1 in establishing developmental RT programs, we next analyzed RT changes between subsequent stages. We compared differences in RT between control morula and 8-cell stage with those between control 8- and 4-cell stage. Genome-wide analysis of RT differences between stages revealed no correlation between changes from 4- to 8-cell stage and changes from 8-cell to morula (Figure S3A). In other words, regions that become replicated earlier at one stage do not become replicated earlier at the subsequent stage (Figure S3A). Likewise for genomic regions replicating later between stages (Figure S3A). This suggests that different genomic regions “mature” their RT toward earlier or later at subsequent developmental stages. This indicates that each stage undergoes a maturation program. We then asked whether RIF1 regulates the same genomic regions at different stages. For this, we compared the differences in RT values across all genomic bins

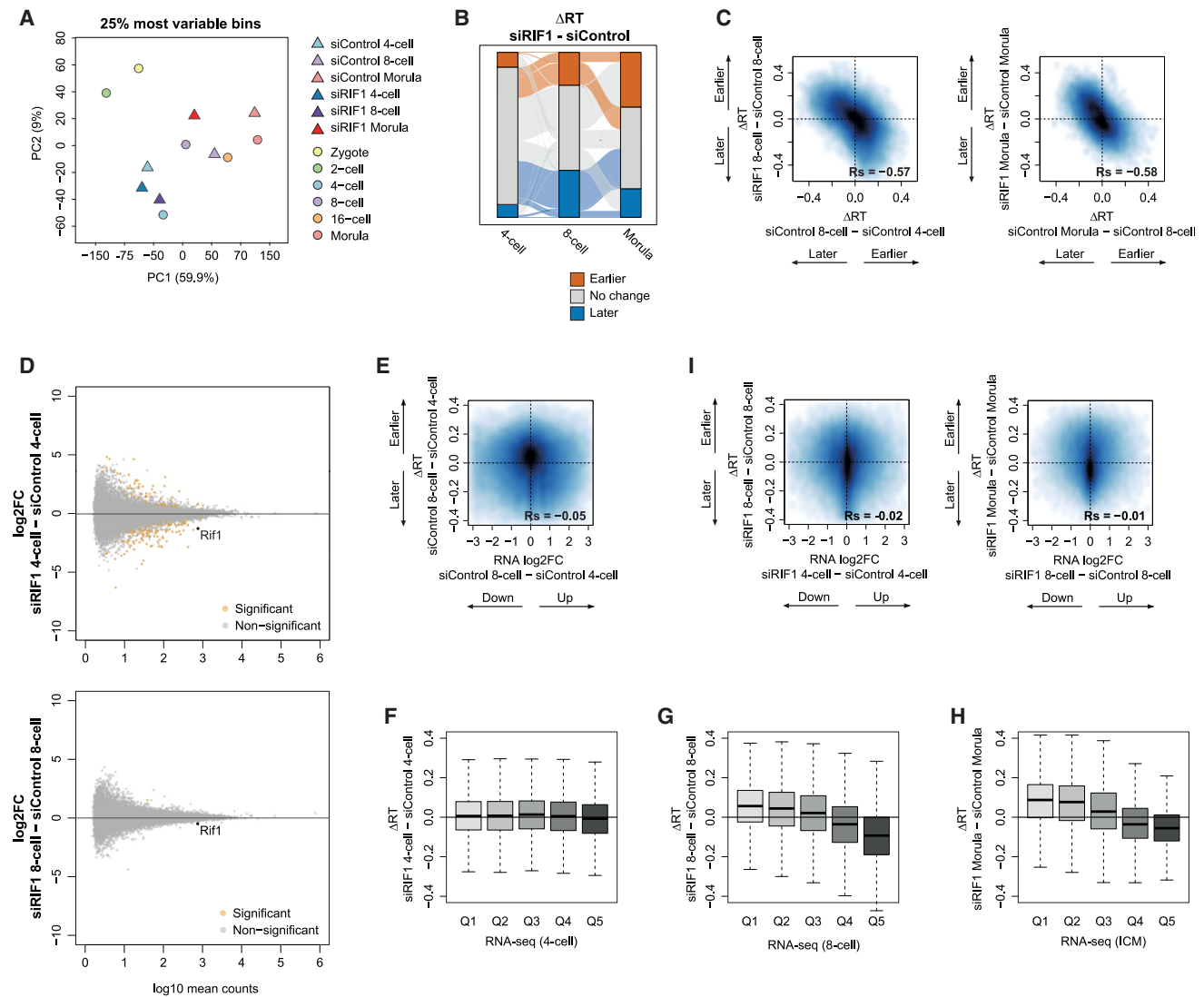


Figure 3. RIF1 depletion prevents changes of RT that would occur between stages without majorly affecting gene expression

(A) Principal-component analysis (PCA) of RT profiles from siControl, siRIF1 embryos, and publicly available wild-type stages. The 25% most variable bins are used.

(B) Alluvial plot showing genomic bins identified as significantly changing to earlier and later RT upon RIF1 depletion, centered at the 8-cell stage, is shown.

(C) Smoothed scatter plot of RT differences (Δ RT) between the same stages of *Rif1* and control siRNA-microinjected embryos versus RT differences (Δ RT) between different stages of control siRNA-injected embryos.

(D) MA plots showing differentially expressed genes between RIF1-depleted and control embryos at 4-cell ($n = 175$ DE genes) and 8-cell stage ($n = 1$ DE gene). p values obtained by DESeq2.

(E) Smoothed scatter plot of RT differences (Δ RT) between 8- and 4-cell stage versus changes in RNA expression (\log_2 FC) between 8- and 4-cell stage in control embryos.

(F) Boxplots depicting RT changes (Δ RT) in genomic bins upon RIF1 depletion according to expression levels (GSE45719⁴⁰), and Q5 corresponds to the highest expression and Q1 to the lowest. Boxplots show median of Δ RT values and IQR, and whiskers depict the smallest and largest values within $1.5 \times$ IQR.

(G) As in (F), but 8-cell stage

(H) As in (F), but morula stage. Expression data from morula are not available, and thus we used inner cell mass (ICM) data.

(I) Smoothed scatterplots of RT differences (Δ RT) between the same stages of RIF1 and control embryos versus changes in RNA expression (\log_2 FC) between RIF1 and control embryos.

In (C), (E), and (I), R_s : Spearman's correlation.

between RIF1-depleted embryos and controls between stages. This indicated that RT changes elicited upon RIF1 depletion at the 8-cell stage are not correlated to those at the 4-cell stage (Figure S3B). In other words, RIF1 regulates the RT program of

these two stages in a stage-specific manner. Interestingly, however, the same analysis between the 8-cell and the morula stage revealed a greater positive correlation (Figure S3B), indicating that while most genomic regions are similarly regulated by

RIF1 at these stages, some other regions are not. These data suggest that RIF1 regulates both shared and stage-specific parts of the RT program in morula and 8-cell stage embryos.

Accordingly, we note that regions that change to later replication in RIF1's absence, for example at the 8-cell stage, are not necessarily changing to later replication at the 4-cell or morula stages (Figure 3B). These observations raise the possibility that RIF1 acts in the *establishment* rather than the *maintenance* of RT once set up. We addressed this by asking if RIF1 regulates RT of those genomic regions in particular, which change RT for the first time between subsequent developmental stages. For this, we compared differences in RT values elicited by RIF1 depletion at the 8-cell stage with differences in RT emerging between the 8- and 4-cell stages. We find that RT changes that occur as development proceeds anticorrelate with RT changes elicited upon RIF1 depletion (Figure 3C). For example, regions shifting toward earlier replication from 4- to 8-cell in control embryos shift toward later replication in 8-cell upon RIF1 depletion (Figures 3C and S3C). We obtained similar results in morula (Figures 3C and S3D). These data indicate that RIF1 depletion affects genomic regions that undergo developmental RT changes and suggest that RIF1 regulates RT changes that emerge normally between developmental stages.

Considering that embryonic transcription fine-tunes the RT program,¹⁰ we next investigated whether RT changes upon RIF1 depletion are associated with transcriptional changes in previous developmental stages. We performed RNA sequencing (RNA-seq) in control and RIF1-depleted 4- and 8-cell stage embryos. RIF1 depletion resulted in 175 misregulated genes in 4-cell embryos but only one gene at the 8-cell stage (Figure 3D; Tables S2 and S3). We found no correlation between differentially expressed genes and RT changes within the same developmental stage: regions that shifted either toward earlier or later replication in the absence of RIF1 did not display changes in transcript abundance (Figure S3E). Thus, changes in RT upon RIF1 loss can occur independently of changes in transcriptional activity, and therefore changes in RT are disconnected from changes in expression patterns globally. In addition, in control embryos, RT differences emerging between 4- and 8-cell stages do not correlate with differences in gene expression between these two stages (Figures 3E and S3F). This indicates that the developmental changes in RT between these two stages are not related to changes in their gene expression profiles.

We next addressed whether RIF1 depletion affects, more specifically, highly transcribed genes. We stratified genomic bins in quintiles based on expression levels in wild-type embryos and calculated the RT differences elicited by RIF1 depletion in each of these quintiles. We find that, at the 4-cell stage, RIF1 depletion does not affect RT of any quintile (Figure 3F). However, at both the 8-cell and morula stages, genomic bins that are more highly transcribed become replicated later in the absence of RIF1 (Figures 3G and 3H). Thus, these data suggest that while changes in gene expression elicited by RIF1 depletion do not necessarily lead to a change in RT, some loci are more sensitive to RIF1 depletion as development proceeds, at the 8-cell and morula stages, and this can correlate with their expression levels.

Lastly, we examined whether changes in RT at the 8-cell stage following RIF1 depletion are related to changes in transcription at

the 4-cell stage but found no correlation between them (Figure 3I). The same analysis comparing RIF1-mediated changes of RT in morula indicated no relationship between changes in transcription at the 8-cell stage (Figure 3I). Overall, these data indicate that developmental RT changes are disentangled from changes in transcription and that the changes elicited upon RIF1 depletion are also unrelated to changes in gene expression. We find these observations particularly relevant since they establish that changes in RT are not necessarily dependent on changes in transcription *in vivo*. Overall, we conclude that RIF1 establishes *de novo*, stage-specific developmental RT programs, which are unrelated to changes in gene expression.

Lamina association and RT are uncoupled upon RIF1 depletion in early embryos

We next explored the relationship between RT established by RIF1 and nuclear organization. In particular, since it has been proposed that early embryonic LADs can prime early and late RT at later developmental stages,¹⁰ we focused on LADs. We asked whether RT changes could be explained by changes in lamina association upon RIF1 depletion at earlier stages. We first investigated whether RIF1 depletion affects nuclear organization by mapping LADs in control and RIF1-depleted 4- and 8-cell stage embryos.^{28,41} We generated laminB1-DamID profiles as before.^{28,31,42} RIF1 depletion led to changes in genome-nuclear lamina interactions at both the 4- and 8-cell stages (Figure 4A). We observed both regions that increased and regions that decreased interactions with the lamina (Figure 4A). The effects of RIF1 depletion were larger at the 8-cell compared with the 4-cell stage (Figure 4A). Such changes in lamina association occur despite virtually no changes in gene expression in RIF1-depleted embryos at the 8-cell stage and only 175 deregulated genes at the 4-cell stage (Figure 3D). While the total number of LADs remained similar between control and RIF1-depleted 8-cell embryos (746 and 738 LADs, respectively), the number of LADs increased upon RIF1 loss at the 4-cell stage (601–644 LADs) (Figure 4B). 4-cell stage LADs displayed a median size of 0.9 Mb (mean 1.30 Mb) in controls, compared with 1.0 Mb (mean 1.61 Mb) in RIF1-depleted embryos (Figure 4B), which overall resulted in a larger proportion of the genome associated with the nuclear lamina at the 4-cell stage upon RIF1 loss (Figure 4C). Indeed, pairwise comparison of LADs and iLADs between controls and RIF1-depleted embryos indicated that RIF1 depletion leads to alterations in LADs at both the 4- and the 8-cell stage (Figure 4D).

We next asked whether RT changes upon RIF1 loss relate to changes in LADs/iLADs. Comparing genome-wide differences in RT between control and RIF1-depleted embryos against differences in lamina association at the 4-cell stage indicated no correlation between changes in RT and nuclear positioning (Figure 4E). We obtained similar results at the 8-cell stage (Figure 4E). Indeed, plotting the changes in RT of regions with significantly increased or decreased LaminB1 DNA adenine methyltransferase identification (DamID) methylation values indicates no changes in RT according to whether a region is repositioned toward or away from the lamina (Figure S4A). Alterations in RT can occur regardless of the direction in which repositioning with respect to the nuclear lamina occurs: regions shifting toward early replication upon RIF1 depletion can both increase and

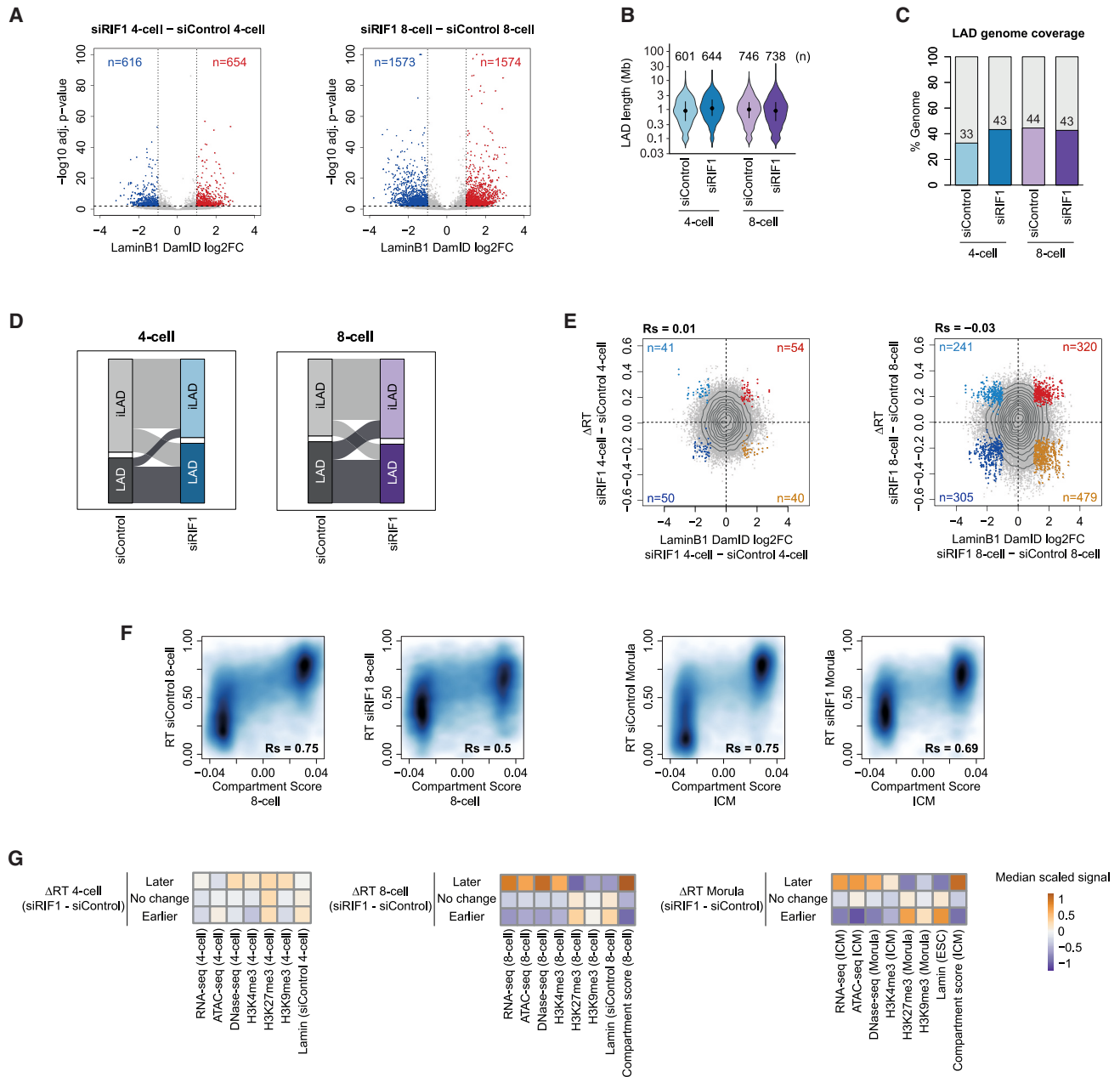


Figure 4. RIF1 controls RT independently of genome-lamina interactions

(A) Volcano plots showing genomic bins with significantly increased (red) and decreased (blue) lamina interactions upon RIF1 depletion. p values calculated from a generalized linear model of the gamma family.

(B) Violin plots of LAD length. The 25th and 75th percentiles (black lines), median (dots), and LAD number (n) are indicated.

(C) Percentage genomic coverage of LADs and iLADs after RIF1 depletion.

(D) Alluvial plots depicting genomic distribution of LADs and iLADs in controls and their changes upon RIF1 depletion.

(E) Scatterplots of RT differences (Δ RT) between the same stages of RIF1-depleted and control embryos versus changes in Dam LaminB1 OE values (log₂FC) between the same stages of RIF1-depleted and control embryos. Contour (black) lines indicate genomic bin density. Number of significantly changed genomic bins in each quadrant is indicated (n) and highlighted as colored dots. R_s : Spearman's correlation.

(F) Smoothed scatterplots showing correlation between RT values of control and RIF1-depleted embryos and Hi-C compartment score of wild-type embryos. Positive compartment scores define A compartment. R_s : Spearman's correlation.

(G) Median enrichment of chromatin features in wild-type embryos at differential RT genomic bins between RIF1-depleted and control embryos. When data from the same stage as RT are not available, the closest stage data are used for analysis.

decrease the strength of their association with the nuclear lamina (Figures 4E and S4B). The same occurs in regions shifting toward late replication in RIF1-depleted embryos (Figures 4E and S4B). This phenotype is more marked in 8-cell embryos compared with 4-cell, presumably because RT changes are larger at the 8-cell stage. We also observed that genomic regions with lower LaminB1 DamID methylation levels in both control and RIF1-depleted embryos shift to later replication upon RIF1 knockdown (Figure S4B, see region ~165 to ~170 Mb). This would suggest a role of RIF1 in RT regulation independently of lamina interactions. Indeed, overall, control 8-cell stage iLADs tend to replicate later upon RIF1 depletion (Figure S4C), and the RT difference between LADs and iLADs becomes more equal in RIF1-depleted embryos (Figure S4D). Thus, there is no strict relationship between RT changes caused by RIF1 loss and changes in lamina association within each developmental stage.

Next, we addressed whether alterations in LADs/iLADs upon RIF1 depletion account for RT changes at the subsequent developmental stage. Genome-wide analysis of RT changes upon RIF1 depletion at the 8-cell stage revealed a positive, yet low correlation with changes in lamina association at the 4-cell stage (Figure S4E). However, this correlation decreased to practically zero when comparing RT changes between control and RIF1-depleted embryos in morula, with changes in LaminB1 DamID methylation levels upon RIF1 loss at the 8-cell stage (Figure S4E). Thus, the association to the nuclear lamina is not a determining factor for the outcome of RT changes upon RIF1 depletion. We conclude that RIF1 regulates RT independently of radial nuclear positioning and that RT and positioning at the nuclear lamina are molecularly disentangled in early embryos. Notably, most regions shifting toward earlier RT upon RIF1 loss have a strong B compartment score, and those shifting toward late have a strong A compartment score (Figure 4F). Indeed, analysis of the chromatin features of genomic regions that change RT upon RIF1 depletion indicates a strong compartment definition in the regions that shift toward earlier or later replication in all developmental stages analyzed (Figure 4G). This is also reflected in the strong demarcation by a higher chromatin accessibility and higher levels of transcripts overall in the regions replicating later upon RIF1 depletion, while the opposite is true for regions replicating earlier, which are characterized by lesser accessibility and less abundant transcriptome (Figure 4G). Accordingly, genomic regions that change RT upon RIF1 depletion toward later are characterized by higher levels of H3K4me3 but lower levels of H3K27me3 and H3K9me3 compared with regions that are not affected by RIF1 loss, and this is both at the 8-cell and morula stages (Figure 4G). By contrast, genomic regions shifting RT toward earlier upon RIF1 depletion are overall enriched in H3K27me3 but depleted of H3K4me3 compared with insensitive-RIF1 regions (Figure 4G). We propose that the organization of the genome into A and B compartments may have a larger influence on RT regulation—or vice versa—than lamina association. This implies that compartments and RT may act as the core factors for chromatin organization during early development.

Finally, we investigated whether RIF1 depletion leads to global changes in histone modifications. Immunostaining for H3K4me3, H3K9me3, and H3K27me3 in morula, stage with the largest RT changes upon RIF1 loss, revealed no detectable changes in

any of these histone modifications in RIF1-depleted embryos compared with controls (Figure S4F).

DISCUSSION

RT is closely linked to the establishment and restoration of chromatin states.^{3,43} Earlier work indicated that RT is not well defined initially, in line with a higher chromatin plasticity at the earliest developmental stages. Our work indicates that the absence of RIF1 prevents the emergence of a consolidated RT program and provides insights into the relationship between RT and nuclear organization as well as transcription.

RIF1 plays multiple roles during replication.^{17,33,44} Phenotypes elicited upon RIF1 depletion in different cell types differ, suggesting cell-type-specific regulation and/or the presence of different regulators in different cells. Apparent phenotypic differences upon RIF1 loss may be due to the use of different cell types and/or the timing at which analyses were performed. For example, mouse fibroblasts without RIF1 show reduced EdU incorporation, suggesting defects in S-phase progression but no detectable phenotype in the proportion of cells in G2/M.¹⁷ They also accumulate DNA damage during S phase.¹⁷ Cornacchia et al. showed that RIF1 deletion in pMEFs increases p21 levels, suggesting a delayed entry into S phase. Whether S-phase progression is regulated by RIF1 in human cells is less clear, as some have shown that S-phase progression remains unaffected in RIF1-depleted HeLa cells,³⁵ while other work indicates that siRIF1 HeLa cells progress more quickly through S phase.⁴⁴ While in mouse fibroblasts, where the G1/S checkpoint is active, RIF1 causes a delay in entry into S phase,³³ in HeLa cells, which are p53 negative, this does not happen,³⁵ nor does it in immortalized fibroblasts, where p53 has been inactivated.¹⁶ In the latter, it is rather the DNA replication checkpoint that is activated upon RIF1 loss. Thus, some of the phenotypes elicited upon RIF1 depletion may depend upon the checkpoint machinery of each cell type.

In *Drosophila*, developmental progression is accompanied by increase in the length of S phase, which is prevented upon RIF1 depletion.³⁴ Imaging cell biology approaches inferred delayed replication of heterochromatin upon RIF1 depletion.³⁴ Similarly, mid-blastula transition in zebrafish is characterized by initial S-phase lengthening and appearance of G2 phase.²² Upon RIF1 depletion, the zebrafish RT program does not mature from the shield to the 24 hours post-fertilization (hpf) stage as in wild-type embryos.²¹ Our work extends these observations to mammals by reporting a role for RIF1 in regulating RT in mouse embryos and provides an in-depth molecular characterization of RT genome-wide and on the impact of RIF1 loss on nuclear organization and transcription.

In contrast to human ESCs, in which cell proliferation is not majorly impaired upon RIF1 depletion, albeit an accumulation of cells with a G2/M DNA content,^{15,16} mouse ESCs show reduced proliferation upon RIF1 knockdown, partly due to decreased cell viability¹⁶ and, accordingly, are unable to form teratomas.⁴⁵ Interestingly, however, mouse ESCs without RIF1 have altered telomere length but without detectable signs of DNA damage, assessed by monitoring γ H2A.X and 53BP1. However, RIF1 knockout mice do not show telomere shortening.¹⁷ The effect on telomeres in RIF1-depleted mouse ESCs

is indirect and results from upregulation of ZSCAN4, which is negatively regulated by RIF1.⁴⁵ Indeed, RIF1 depletion in mouse ESCs results in upregulation of *Zscan4* and of a “2C” transcriptional program.^{46,47} This contrasts with our results in mouse embryos, in which there are no detectable changes in *Zscan4* upon RIF1 depletion. In fact, RT changes in embryos upon RIF1 depletion occur largely in the absence of changes in transcription. Our data indicate that RIF1 regulates RT maturation at the times during development when cell fates are acquired and that these RT changes are unrelated to the transcriptional changes typical of those new cell identities. In human ESCs, RIF1 depletion leads to only a few affected (~50) genes in the first cell cycle after depletion, but different genes are affected in different cells.¹⁵ Upon further cell cycle passages, ~2,000 genes become affected, which tend to be more consistent between cells, suggesting that transcriptional changes result primarily from several cycles of disrupted RT and that continued proliferation in the absence of RIF1 induces progressive gene deregulation.

Our data suggest that the genome also reorganizes in the absence of RIF1, with altered LAD/iLAD boundaries and changes in nuclear lamina interactions of several LADs and iLADs. A change in chromatin architecture was also observed in mouse ESCs, where RIF1 mediates inter-replication domain contacts.¹⁶ In B cells, RIF1 promotes early replication but has minor effects on gene expression and genome organization.¹³ Thus, these findings add to the observations that these two pillars of nuclear organization—radial positioning toward the nuclear lamina and RT—can be disentangled.

Preventing RT consolidation (through RIF1 depletion) leads to slower fork speed, a feature observed at earlier developmental stages.³² This suggests that RT consolidation may be related to the speed at which DNA replication occurs and potentially to the number of origins fired. However, it is currently impossible to ascertain whether these features are causally related or whether they are two separate features that co-occur phenotypically in totipotent cells of early embryos.

The expression pattern of RIF1 in the early embryo alone may explain the developmental consolidation of RT. RNAi screenings in mouse ESCs identified RIF1 as a protein regulating reprogramming toward 2-cell-like cells (2CLCs).^{45,47,48} Expression of RIF1 lacking the N terminus HEAT repeat induces 2CLCs through a dominant negative effect, presumably by competing endogenous, full-length RIF1 function.⁴⁸ Mouse oocytes express multiple short isoforms primarily derived from the N terminus of RIF1 and only a small fraction of full-length RIF1.¹⁴ This is similar in 2-cell embryos, but the proportion of full-length RIF1 increases drastically at the morula stage. While we cannot rule out the existence of additional functional isoforms, undetectable with currently available antibodies, our data suggest that the emergence of a more consolidated RT program correlates with RIF1 detection in the nucleus, from the 4-cell stage.¹⁴ Thus, embryos may have evolved an effective mechanism to regulate RT consolidation through developmentally regulating isoforms and localization of RIF1. We propose that a less consolidated RT program is promoted by the differential isoform localization of RIF1.

The effects of RIF1 depletion at the 4-cell stage are milder compared with cell culture systems.¹⁵ This may be linked to the biology of the mammalian embryo, considering that

zygotes and 2-cell embryos possess a very distinctive RT program.^{10,49,50} By contrast, as development proceeds, when embryos display a more consolidated RT program, effects upon RIF1 loss are larger. Whether other factors contribute to further control RT and/or whether the distinctive chromatin configuration of early embryos renders the RT more robust to RIF1 perturbation remains to be investigated. Phenotypic differences between embryos and cultured cells also highlight the importance of investigating regulatory mechanisms during embryogenesis *in vivo*, in physiologically relevant contexts.

Limitations of the study

We use scRepli-seq because blastomeres are asynchronous and because low-input approaches are required. scRepli-seq data are of relatively low resolution (50 kb), and individual replication origins cannot be defined. Origin mapping would greatly propel our understanding of DNA replication during development. While all features of the RT program we report are consistent with a less coordinated and altered RT in embryos, we cannot formally rule out that the increase in T_{width} , and thus heterogeneity, may be due to the sampling of cells with lower RIF1 depletion. Because siRNA may not target all potential isoforms of *Rif1*, the role that we document for RIF1 may be underestimated. Also, our immunostaining suggests that RIF1 depletion does not lead to global disruption of histone modifications analyzed, but changes at specific genomic loci cannot be ruled out. The embryo-specific phenotypic outcome upon RIF1 depletion remains to be studied. For this, mass spectrometry to identify RIF1-interacting partners is a plausible approach in cells in culture but is unlikely to yield robust data in early embryos in which the amount of material is limiting. Finally, our observations that RIF1 depletion does not affect developmental progression until the blastocyst stage leave a long-standing open question, as it remains unclear whether and how essential the RT program is for development.

RESOURCE AVAILABILITY

Lead contact

Further information should be directed to the lead contact, Maria-Elena Torres-Padilla (torres-padilla@helmholtz-muenchen.de).

Materials availability

No new materials were generated in this study.

Data and code availability

- Data are available through GSE262791.
- Original code and corresponding pipeline⁵¹ through gitlab (https://ascgitlab.helmholtz-muenchen.de/public_pipelines/repliseq_rif1).
- Additional information required to reanalyze the data reported in this work paper is available upon request. The scRepli-seq, RNA-seq, and DamID-seq data from this study are available from the Gene Expression Omnibus, accession number GSE262791. The code used for scRepli-seq and DamID analysis can be accessed here: https://ascgitlab.helmholtz-muenchen.de/public_pipelines/repliseq_rif1.

ACKNOWLEDGMENTS

We thank I. de la Rosa Velazquez (Sequencing Facility Helmholtz Munich), A. Burton, and S. Hamperl for manuscript reading and N. Yoshizawa-Sugata and H. Masai for RIF1 antibody. M.-E.T.-P. acknowledges funding by Helmholtz

Association, German Research Foundation (DFG) project-ID 213249687 (SFB 1064), and NIH 4DN program (grant number 5 U01DK127391-03). M.P. and M.-E.T.-P. acknowledge support from the Horizon 2020 Marie Skłodowska-Curie grant agreement “ChromDesign” (813327) and D.M.G. from NIH (grant number R01GM083337).

AUTHOR CONTRIBUTIONS

T.N. designed, performed, and analyzed most experiments. T.S. performed all bioinformatics. M.P. performed DamID experiments and contributed to their bioinformatic analysis. A.E. performed image analyses. L.A.-P. contributed to code generation. J.Z. provided animal protocol expertise toward approval by the Regierung von Oberbayern. D.M.G. provided study support. M.-E.T.-P. conceived, designed, and supervised the study. All authors contributed to manuscript preparation and read, commented, and approved the manuscript.

DECLARATION OF INTERESTS

M.-E.T.-P. is a member of the ethics advisory panel of MERCK.

STAR★METHODS

Detailed methods are provided in the online version of this paper and include the following:

- KEY RESOURCES TABLE
- EXPERIMENTAL MODEL AND STUDY PARTICIPANT DETAILS
 - Embryo collection and culture
- METHOD DETAILS
 - Immunostaining
 - Quantification of RIF1 fluorescence intensity in 3D
 - DNA fibres
 - Repli-seq
 - scRepli-seq read alignment and quality control filtering
 - Assignment of replication status
 - Replication score, bin-bin distance, replication timing value and variability score
 - Identification of IZs (RT peaks), TTRs and TZs (RT troughs)
 - Analysis of RT heterogeneity
 - scRepli-seq statistical analysis
 - Single embryo RNA-seq and library preparation
 - RNA-seq analysis
 - DamID-sequencing and analysis
 - Analysis of public chromatin datasets
 - Analysis of publicly available RNA-seq datasets
 - Analysis of public Hi-C dataset
 - Image analysis of morula and blastocyst stage embryos
- QUANTIFICATION AND STATISTICAL ANALYSIS

SUPPLEMENTAL INFORMATION

Supplemental information can be found online at <https://doi.org/10.1016/j.devcel.2025.03.016>.

Received: April 4, 2024
Revised: August 18, 2024
Accepted: March 31, 2025
Published: April 21, 2025

REFERENCES

1. Aladjem, M.I., Rodewald, L.W., Lin, C.M., Bowman, S., Cimbora, D.M., Brody, L.L., Epner, E.M., Groudine, M., and Wahl, G.M. (2002). Replication initiation patterns in the beta-globin loci of totipotent and differentiated murine cells: evidence for multiple initiation regions. *Mol. Cell Biol.* 22, 442–452. <https://doi.org/10.1128/MCB.22.2.442-452.2002>.
2. Ryba, T., Hiratani, I., Sasaki, T., Battaglia, D., Kulik, M., Zhang, J., Dalton, S., and Gilbert, D.M. (2011). Replication timing: a fingerprint for cell identity and pluripotency. *PLOS Comput. Biol.* 7, e1002225. <https://doi.org/10.1371/journal.pcbi.1002225>.
3. Alvarez, V., Bandau, S., Jiang, H., Rios-Szwed, D., Hukelmann, J., Garcia-Wilson, E., Wiechens, N., Griesser, E., Ten Have, S., Owen-Hughes, T., et al. (2023). Proteomic profiling reveals distinct phases to the restoration of chromatin following DNA replication. *Cell Rep.* 42, 111996. <https://doi.org/10.1016/j.celrep.2023.111996>.
4. Alabert, C., Bukowski-Wills, J.C., Lee, S.B., Kustatscher, G., Nakamura, K., de Lima Alves, F., Menard, P., Mejlvang, J., Rappsilber, J., and Groth, A. (2014). Nascent chromatin capture proteomics determines chromatin dynamics during DNA replication and identifies unknown fork components. *Nat. Cell Biol.* 16, 281–293. <https://doi.org/10.1038/ncb2918>.
5. Hiratani, I., Ryba, T., Itoh, M., Yokochi, T., Schwaiger, M., Chang, C.W., Lyou, Y., Townes, T.M., Schübeler, D., and Gilbert, D.M. (2008). Global reorganization of replication domains during embryonic stem cell differentiation. *PLoS Biol.* 6, e245. <https://doi.org/10.1371/journal.pbio.0060245>.
6. Fragkos, M., Ganier, O., Coulombe, P., and Méchali, M. (2015). DNA replication origin activation in space and time. *Nat. Rev. Mol. Cell Biol.* 16, 360–374. <https://doi.org/10.1038/nrm4002>.
7. Dimitrova, D.S., and Gilbert, D.M. (1999). The spatial position and replication timing of chromosomal domains are both established in early G1 phase. *Mol. Cell* 4, 983–993. [https://doi.org/10.1016/s1097-2765\(00\)80227-0](https://doi.org/10.1016/s1097-2765(00)80227-0).
8. Zhao, P.A., Sasaki, T., and Gilbert, D.M. (2020). High-resolution Repli-Seq defines the temporal choreography of initiation, elongation and termination of replication in mammalian cells. *Genome Biol.* 21, 76. <https://doi.org/10.1186/s13059-020-01983-8>.
9. Wang, W., Klein, K.N., Proesmans, K., Yang, H., Marchal, C., Zhu, X., Borrmann, T., Hastie, A., Weng, Z., Bechhoefer, J., et al. (2021). Genome-wide mapping of human DNA replication by optical replication mapping supports a stochastic model of eukaryotic replication. *Mol. Cell* 81, 2975–2988.e6. <https://doi.org/10.1016/j.molcel.2021.05.024>.
10. Nakatani, T., Schauer, T., Altamirano-Pacheco, L., Klein, K.N., Ettinger, A., Pal, M., Gilbert, D.M., and Torres-Padilla, M.E. (2024). Emergence of replication timing during early mammalian development. *Nature* 625, 401–409. <https://doi.org/10.1038/s41586-023-06872-1>.
11. Xu, S., Wang, N., Zuccaro, M.V., Gerhardt, J., Baslan, T., Koren, A., and Egli, D. (2023). DNA replication in early mammalian embryos is patterned, predisposing lamina-associated regions to fragility. Preprint at bioRxiv. <https://doi.org/10.1101/2023.12.25.573304>.
12. Peace, J.M., Ter-Zakarian, A., and Aparicio, O.M. (2014). Rif1 regulates initiation timing of late replication origins throughout the *S. cerevisiae* genome. *PLoS One* 9, e98501. <https://doi.org/10.1371/journal.pone.0098501>.
13. Malz, D., Peycheva, M., Rahjouei, A., Gnan, S., Klein, K.N., Nazarova, M., Schoeberl, U.E., Gilbert, D.M., Buonomo, S.C.B., Di Virgilio, M., et al. (2023). RIF1 regulates early replication timing in murine B cells. *Nat. Commun.* 14, 8049. <https://doi.org/10.1038/s41467-023-43778-y>.
14. Yoshizawa-Sugata, N., Yamazaki, S., Mita-Yoshida, K., Ono, T., Nishito, Y., and Masai, H. (2021). Loss of full-length DNA replication regulator Rif1 in two-cell embryos is associated with zygotic transcriptional activation. *J. Biol. Chem.* 297, 101367. <https://doi.org/10.1016/j.jbc.2021.101367>.
15. Klein, K.N., Zhao, P.A., Lyu, X., Sasaki, T., Bartlett, D.A., Singh, A.M., Tasan, I., Zhang, M., Watts, L.P., Hiraga, S.I., et al. (2021). Replication timing maintains the global epigenetic state in human cells. *Science* 372, 371–378. <https://doi.org/10.1126/science.aba5545>.
16. Foti, R., Gnan, S., Cornacchia, D., Dileep, V., Bulut-Karsioglu, A., Diehl, S., Buness, A., Klein, F.A., Huber, W., Johnstone, E., et al. (2016). Nuclear Architecture Organized by Rif1 Underpins the Replication-Timing Program. *Mol. Cell* 61, 260–273. <https://doi.org/10.1016/j.molcel.2015.12.001>.

17. Buonomo, S.B.C., Wu, Y., Ferguson, D., and de Lange, T. (2009). Mammalian Rif1 contributes to replication stress survival and homology-directed repair. *J. Cell Biol.* *187*, 385–398. <https://doi.org/10.1083/jcb.200902039>.
18. Chapman, J.R., Barral, P., Vannier, J.B., Borel, V., Steger, M., Tomas-Loba, A., Sartori, A.A., Adams, I.R., Batista, F.D., and Boulton, S.J. (2013). RIF1 is essential for 53BP1-dependent nonhomologous end joining and suppression of DNA double-strand break resection. *Mol. Cell* *49*, 858–871. <https://doi.org/10.1016/j.molcel.2013.01.002>.
19. Daxinger, L., Harten, S.K., Oey, H., Epp, T., Isbel, L., Huang, E., Whitelaw, N., Apedaille, A., Sorolla, A., Yong, J., et al. (2013). An ENU mutagenesis screen identifies novel and known genes involved in epigenetic processes in the mouse. *Genome Biol.* *14*, R96. <https://doi.org/10.1186/gb-2013-14-9-r96>.
20. Enervald, E., Powell, L.M., Boteva, L., Foti, R., Blanes Ruiz, N., Kibar, G., Piszczek, A., Cavaleri, F., Vingron, M., Cerase, A., et al. (2021). RIF1 and KAP1 differentially regulate the choice of inactive versus active X chromosomes. *EMBO J.* *40*, e105862. <https://doi.org/10.15252/embj.2020105862>.
21. Masser, E.A., N.T., Siefert, J.C., Goins, D., Sansam, C.G., and Sansam, C.L. (2023). Zebrafish Rif1 impacts zygotic genome activation, replication timing, and sex determination. *eLife* *12*, RP87671.
22. Siefert, J.C., Georgescu, C., Wren, J.D., Koren, A., and Sansam, C.L. (2017). DNA replication timing during development anticipates transcriptional programs and parallels enhancer activation. *Genome Res.* *27*, 1406–1416. <https://doi.org/10.1101/gr.218602.116>.
23. Adams, I.R., and McLaren, A. (2004). Identification and characterisation of mRif1: a mouse telomere-associated protein highly expressed in germ cells and embryo-derived pluripotent stem cells. *Dev. Dyn.* *229*, 733–744. <https://doi.org/10.1002/dvdy.10471>.
24. Pope, B.D., Ryba, T., Dileep, V., Yue, F., Wu, W., Denas, O., Vera, D.L., Wang, Y., Hansen, R.S., Canfield, T.K., et al. (2014). Topologically associating domains are stable units of replication-timing regulation. *Nature* *515*, 402–405. <https://doi.org/10.1038/nature13986>.
25. Moindrot, B., Audit, B., Klous, P., Baker, A., Thermes, C., de Laat, W., Bouvet, P., Mongelard, F., and Arneodo, A. (2012). 3D chromatin conformation correlates with replication timing and is conserved in resting cells. *Nucleic Acids Res.* *40*, 9470–9481. <https://doi.org/10.1093/nar/gks736>.
26. Yaffe, E., Farkash-Amar, S., Polten, A., Yakhini, Z., Tanay, A., and Simon, I. (2010). Comparative analysis of DNA replication timing reveals conserved large-scale chromosomal architecture. *PLoS Genet.* *6*, e1001011. <https://doi.org/10.1371/journal.pgen.1001011>.
27. Chen, N., and Buonomo, S.C.B. (2023). Three-dimensional nuclear organisation and the DNA replication timing program. *Curr. Opin. Struct. Biol.* *83*, 102704. <https://doi.org/10.1016/j.sbi.2023.102704>.
28. Borsos, M., Perricone, S.M., Schauer, T., Pontabry, J., de Luca, K.L., de Vries, S.S., Ruiz-Morales, E.R., Torres-Padilla, M.E., and Kind, J. (2019). Genome-lamina interactions are established de novo in the early mouse embryo. *Nature* *569*, 729–733. <https://doi.org/10.1038/s41586-019-1233-0>.
29. Ke, Y., Xu, Y., Chen, X., Feng, S., Liu, Z., Sun, Y., Yao, X., Li, F., Zhu, W., Gao, L., et al. (2017). 3D Chromatin Structures of Mature Gametes and Structural Reprogramming during Mammalian Embryogenesis. *Cell* *170*, 367–381.e20. <https://doi.org/10.1016/j.cell.2017.06.029>.
30. Du, Z., Zheng, H., Huang, B., Ma, R., Wu, J., Zhang, X., He, J., Xiang, Y., Wang, Q., Li, Y., et al. (2017). Allelic reprogramming of 3D chromatin architecture during early mammalian development. *Nature* *547*, 232–235. <https://doi.org/10.1038/nature23263>.
31. Pal, M., Altamirano-Pacheco, L., Schauer, T., and Torres-Padilla, M.E. (2023). Reorganization of lamina-associated domains in early mouse embryos is regulated by RNA polymerase II activity. *Genes Dev.* *37*, 901–912. <https://doi.org/10.1101/gad.350799.123>.
32. Nakatani, T., Lin, J., Ji, F., Ettinger, A., Pontabry, J., Tokoro, M., Altamirano-Pacheco, L., Fiorentino, J., Mahammadov, E., Hatano, Y., et al. (2022). DNA replication fork speed underlies cell fate changes and promotes reprogramming. *Nat. Genet.* *54*, 318–327. <https://doi.org/10.1038/s41588-022-01023-0>.
33. Cornacchia, D., Dileep, V., Quivy, J.P., Foti, R., Tili, F., Santarella-Mellwig, R., Antony, C., Almouzni, G., Gilbert, D.M., and Buonomo, S.B.C. (2012). Mouse Rif1 is a key regulator of the replication-timing programme in mammalian cells. *EMBO J.* *31*, 3678–3690. <https://doi.org/10.1038/emboj.2012.214>.
34. Seller, C.A., and O'Farrell, P.H. (2018). Rif1 prolongs the embryonic S phase at the *Drosophila* mid-blastula transition. *PLoS Biol.* *16*, e2005687. <https://doi.org/10.1371/journal.pbio.2005687>.
35. Yamazaki, S., Ishii, A., Kanoh, Y., Oda, M., Nishito, Y., and Masai, H. (2012). Rif1 regulates the replication timing domains on the human genome. *EMBO J.* *31*, 3667–3677. <https://doi.org/10.1038/emboj.2012.180>.
36. Fernandez-Capetillo, O., Lee, A., Nussenzweig, M., and Nussenzweig, A. (2004). H2AX: the histone guardian of the genome. *DNA Repair (Amst)* *3*, 959–967. <https://doi.org/10.1016/j.dnarep.2004.03.024>.
37. Xu, L., and Blackburn, E.H. (2004). Human Rif1 protein binds aberrant telomeres and aligns along anaphase midzone microtubules. *J. Cell Biol.* *167*, 819–830. <https://doi.org/10.1083/jcb.200408181>.
38. Dileep, V., and Gilbert, D.M. (2018). Single-cell replication profiling to measure stochastic variation in mammalian replication timing. *Nat. Commun.* *9*, 427. <https://doi.org/10.1038/s41467-017-02800-w>.
39. Palmerola, K.L., Amrane, S., De Los Angeles, A., Xu, S., Wang, N., de Pinho, J., Zuccaro, M.V., Tagliatela, A., Massey, D.J., Turocy, J., et al. (2022). Replication stress impairs chromosome segregation and preimplantation development in human embryos. *Cell* *185*, 2988–3007.e20. <https://doi.org/10.1016/j.cell.2022.06.028>.
40. Deng, Q., Ramsköld, D., Reinius, B., and Sandberg, R. (2014). Single-cell RNA-seq reveals dynamic, random monoallelic gene expression in mammalian cells. *Science* *343*, 193–196. <https://doi.org/10.1126/science.1245316>.
41. Greil, F., Moorman, C., and van Steensel, B. (2006). DamID: mapping of in vivo protein-genome interactions using tethered DNA adenine methyltransferase. *Methods Enzymol.* *410*, 342–359. [https://doi.org/10.1016/S0076-6879\(06\)10016-6](https://doi.org/10.1016/S0076-6879(06)10016-6).
42. Kind, J., Pagie, L., Ortabozkoyun, H., Boyle, S., de Vries, S.S., Janssen, H., Amendola, M., Nolen, L.D., Bickmore, W.A., and van Steensel, B. (2013). Single-cell dynamics of genome-nuclear lamina interactions. *Cell* *153*, 178–192. <https://doi.org/10.1016/j.cell.2013.02.028>.
43. Alabert, C., and Groth, A. (2012). Chromatin replication and epigenome maintenance. *Nat. Rev. Mol. Cell Biol.* *13*, 153–167. <https://doi.org/10.1038/nrm3288>.
44. Alver, R.C., Chadha, G.S., Gillespie, P.J., and Blow, J.J. (2017). Reversal of DDK-Mediated MCM Phosphorylation by Rif1-PP1 Regulates Replication Initiation and Replisome Stability Independently of ATR/Chk1. *Cell Rep.* *18*, 2508–2520. <https://doi.org/10.1016/j.celrep.2017.02.042>.
45. Dan, J., Liu, Y., Liu, N., Chiourea, M., Okuka, M., Wu, T., Ye, X., Mou, C., Wang, L., Wang, L., et al. (2014). Rif1 maintains telomere length homeostasis of ESCs by mediating heterochromatin silencing. *Dev. Cell* *29*, 7–19. <https://doi.org/10.1016/j.devcel.2014.03.004>.
46. Liu, C., Yu, P., Ren, Z., Yao, F., Wang, L., Hu, G., Li, P., and Zhao, Q. (2023). Rif1 Regulates Self-Renewal and Impedes Mesendodermal Differentiation of Mouse Embryonic Stem Cells. *Stem Cell Rev. Rep.* *19*, 1540–1553. <https://doi.org/10.1007/s12015-023-10525-1>.
47. Rodriguez-Terrones, D., Gaume, X., Ishiuchi, T., Weiss, A., Kopp, A., Kruse, K., Penning, A., Vaquerizas, J.M., Brino, L., and Torres-Padilla, M.E. (2018). A molecular roadmap for the emergence of early-embryonic-like cells in culture. *Nat. Genet.* *50*, 106–119. <https://doi.org/10.1038/s41588-017-0016-5>.
48. Li, P., Wang, L., Bennett, B.D., Wang, J., Li, J., Qin, Y., Takaku, M., Wade, P.A., Wong, J., and Hu, G. (2017). Rif1 promotes a repressive chromatin

- state to safeguard against endogenous retrovirus activation. *Nucleic Acids Res.* 45, 12723–12738. <https://doi.org/10.1093/nar/gkx884>.
49. Halliwell, J.A., Martin-Gonzalez, J., Hashim, A., Dahl, J.A., Hoffmann, E.R., and Lerdrup, M. (2024). Sex-specific DNA-replication in the early mammalian embryo. *Nat. Commun.* 15, 6323. <https://doi.org/10.1038/s41467-024-50727-w>.
50. Xu, S., Wang, N., Zuccaro, M.V., Gerhardt, J., Iyyappan, R., Scatolin, G.N., Jiang, Z., Baslan, T., Koren, A., and Egli, D. (2024). DNA replication in early mammalian embryos is patterned, predisposing lamina-associated regions to fragility. *Nat. Commun.* 15, 5247. <https://doi.org/10.1038/s41467-024-49565-7>.
51. Mölder, F., Jablonski, K.P., Letcher, B., Hall, M.B., Tomkins-Tinch, C.H., Sochat, V., Forster, J., Lee, S., Twardziok, S.O., Kanitz, A., et al. (2021). Sustainable data analysis with Snakemake. *F1000Res* 10, 33. <https://doi.org/10.12688/f1000research.29032.2>.
52. Wu, J., Huang, B., Chen, H., Yin, Q., Liu, Y., Xiang, Y., Zhang, B., Liu, B., Wang, Q., Xia, W., et al. (2016). The landscape of accessible chromatin in mammalian preimplantation embryos. *Nature* 534, 652–657. <https://doi.org/10.1038/nature18606>.
53. Zhang, B., Zheng, H., Huang, B., Li, W., Xiang, Y., Peng, X., Ming, J., Wu, X., Zhang, Y., Xu, Q., et al. (2016). Allelic reprogramming of the histone modification H3K4me3 in early mammalian development. *Nature* 537, 553–557. <https://doi.org/10.1038/nature19361>.
54. Wang, C., Liu, X., Gao, Y., Yang, L., Li, C., Liu, W., Chen, C., Kou, X., Zhao, Y., Chen, J., et al. (2018). Reprogramming of H3K9me3-dependent heterochromatin during mammalian embryo development. *Nat. Cell Biol.* 20, 620–631. <https://doi.org/10.1038/s41556-018-0093-4>.
55. Liu, X., Wang, C., Liu, W., Li, J., Li, C., Kou, X., Chen, J., Zhao, Y., Gao, H., Wang, H., et al. (2016). Distinct features of H3K4me3 and H3K27me3 chromatin domains in pre-implantation embryos. *Nature* 537, 558–562. <https://doi.org/10.1038/nature19362>.
56. Langmead, B., and Salzberg, S.L. (2012). Fast gapped-read alignment with Bowtie 2. *Nat. Methods* 9, 357–359. <https://doi.org/10.1038/nmeth.1923>.
57. Danecek, P., Bonfield, J.K., Liddle, J., Marshall, J., Ohan, V., Pollard, M.O., Whitwham, A., Keane, T., McCarthy, S.A., Davies, R.M., et al. (2021). Twelve years of SAMtools and BCFtools. *GigaScience* 10, giab008. <https://doi.org/10.1093/gigascience/giab008>.
58. Quinlan, A.R., and Hall, I.M. (2010). BEDTools: a flexible suite of utilities for comparing genomic features. *Bioinformatics* 26, 841–842. <https://doi.org/10.1093/bioinformatics/btq033>.
59. Dobin, A., Davis, C.A., Schlesinger, F., Drenkow, J., Zaleski, C., Jha, S., Batut, P., Chaisson, M., and Gingeras, T.R. (2013). STAR: ultrafast universal RNA-seq aligner. *Bioinformatics* 29, 15–21. <https://doi.org/10.1093/bioinformatics/bts635>.
60. Huber, W., Carey, V.J., Gentleman, R., Anders, S., Carlson, M., Carvalho, B.S., Bravo, H.C., Davis, S., Gatto, L., Girke, T., et al. (2015). Orchestrating high-throughput genomic analysis with Bioconductor. *Nat. Methods* 12, 115–121. <https://doi.org/10.1038/nmeth.3252>.
61. Nilsen, G., Liestøl, K., Van Loo, P., Moen Vollan, H.K., Eide, M.B., Rueda, O.M., Chin, S.F., Russell, R., Baumbusch, L.O., Caldas, C., et al. (2012). Copynumber: Efficient algorithms for single- and multi-track copy number segmentation. *BMC Genomics* 13, 591. <https://doi.org/10.1186/1471-2164-13-591>.
62. Benaglia, T. (2009). Mixtools: an R Package for Analyzing Finite Mixture Models. *J. Stat. Softw.* 32, 1–29.
63. Schindelin, J., Arganda-Carreras, I., Frise, E., Kaynig, V., Longair, M., Pietzsch, T., Preibisch, S., Rueden, C., Saalfeld, S., Schmid, B., et al. (2012). Fiji: an open-source platform for biological-image analysis. *Nat. Methods* 9, 676–682. <https://doi.org/10.1038/nmeth.2019>.
64. Stringer, C., and Pachitariu, M. (2024). Cellpose3: one-click image restoration for improved cellular segmentation. *bioRxiv*. Preprint at. <https://doi.org/10.1101/2024.02.10.579780>.
65. Stringer, C., Wang, T., Michaelos, M., and Pachitariu, M. (2021). Cellpose: a generalist algorithm for cellular segmentation. *Nat. Methods* 18, 100–106. <https://doi.org/10.1038/s41592-020-01018-x>.
66. van der Walt, S., Schönberger, J.L., Nunez-Iglesias, J., Boulogne, F., Warner, J.D., Yager, N., Gouillart, E., and Yu, T.; scikit-image contributors (2014). scikit-image: image processing in Python. *PeerJ* 2, e453. <https://doi.org/10.7717/peerj.453>.
67. Técher, H., Koundrioukoff, S., Azar, D., Wilhelm, T., Carignon, S., Brison, O., Debatisse, M., and Le Tallec, B. (2013). Replication dynamics: biases and robustness of DNA fiber analysis. *J. Mol. Biol.* 425, 4845–4855. <https://doi.org/10.1016/j.jmb.2013.03.040>.
68. Conti, C., Saccà, B., Herrick, J., Lalou, C., Pommier, Y., and Bensimon, A. (2007). Replication fork velocities at adjacent replication origins are coordinately modified during DNA replication in human cells. *Mol. Biol. Cell* 18, 3059–3067. <https://doi.org/10.1091/mbc.e06-08-0689>.
69. Tankyevych, O., Talbot, H., and Dokladal, P. (2008). Curvilinear morpho-Hessian filter. In *Internal Symposium on Biomedical imaging: From Nano to Macro (ISBI)*, pp. 1011–1014. <https://doi.org/10.1109/ISBI.2008.4541170>.
70. Breiman, L., Friedman, J., Stone, C., and Olshen, R. (1984). *Classification and Regression Trees* (CRC Press).
71. Bartlett, D.A., Dileep, V., Baslan, T., and Gilbert, D.M. (2022). Mapping Replication Timing in Single Mammalian Cells. *Curr. Protoc.* 2, e334. <https://doi.org/10.1002/cpz1.334>.
72. Takahashi, S., Miura, H., Shibata, T., Nagao, K., Okumura, K., Ogata, M., Obuse, C., Takebayashi, S.I., and Hiratani, I. (2019). Genome-wide stability of the DNA replication program in single mammalian cells. *Nat. Genet.* 51, 529–540. <https://doi.org/10.1038/s41588-019-0347-5>.
73. Efron, B. (1982). The Jackknife, the Bootstrap and Other Resampling Plans. In *CBMS-NSF Regional Conference Series in Applied Mathematics, Monograph 38*. <https://doi.org/10.1137/1.9781611970319>.
74. Picelli, S., Faridani, O.R., Björklund, A.K., Winberg, G., Sagasser, S., and Sandberg, R. (2014). Full-length RNA-seq from single cells using Smart-seq2. *Nat. Protoc.* 9, 171–181. <https://doi.org/10.1038/nprot.2014.006>.
75. Pal, M., Kind, J., and Torres-Padilla, M.E. (2021). DamID to Map Genome-Protein Interactions in Preimplantation Mouse Embryos. *Methods Mol. Biol.* 2214, 265–282. https://doi.org/10.1007/978-1-0716-0958-3_18.
76. Kind, J., Pagie, L., de Vries, S.S., Nahidiazar, L., Dey, S.S., Bienko, M., Zhan, Y., Lajoie, B., de Graaf, C.A., Amendola, M., et al. (2015). Genome-wide maps of nuclear lamina interactions in single human cells. *Cell* 163, 134–147. <https://doi.org/10.1016/j.cell.2015.08.040>.
77. Filion, G.J., van Bommel, J.G., Braunschweig, U., Talhout, W., Kind, J., Ward, L.D., Brugman, W., de Castro, I.J., Kerkhoven, R.M., Bussemaker, H.J., et al. (2010). Systematic protein location mapping reveals five principal chromatin types in *Drosophila* cells. *Cell* 143, 212–224. <https://doi.org/10.1016/j.cell.2010.09.009>.
78. Abe, K., Schauer, T., and Torres-Padilla, M.E. (2022). Distinct patterns of RNA polymerase II and transcriptional elongation characterize mammalian genome activation. *Cell Rep.* 41, 111865. <https://doi.org/10.1016/j.celrep.2022.111865>.
79. Berg, S., Kutra, D., Kroeger, T., Straehle, C.N., Kausler, B.X., Haubold, C., Schiegg, M., Ales, J., Beier, T., Rudy, M., et al. (2019). ilastik: interactive machine learning for (bio)image analysis. *Nat. Methods* 16, 1226–1232. <https://doi.org/10.1038/s41592-019-0582-9>.

STAR★METHODS

KEY RESOURCES TABLE

REAGENT or RESOURCE	SOURCE	IDENTIFIER
Antibodies		
Rabbit anti-mRif1 UCRIII (1673-1851 aa) antiserum	Yoshizawa-Sugata et al. ¹⁴ Tokyo Metropolitan Institute of Medical Science, Tokyo, Japan	https://www.ncbi.nlm.nih.gov/pmc/articles/PMC8686075/
Mouse anti-γH2AX antibody	Abcam	Ab22551, RRID:AB_447150
Mouse anti-IdU antibody	BD Biosciences	347580, RRID:AB_10015219
Rat anti-CldU antibody	Abcam	Ab6326, RRID:AB_305426
Rabbit anti-Histone H3 (tri methyl K4) antibody	EpiCypher	13-0041, RRID:AB_3076423
Rabbit anti-Histone H3 (tri methyl K9) antibody	Abcam	ab8898, RRID:AB_306848
Rabbit anti-Histone H3 (tri methyl K27) antibody	Sigma-Aldrich	07-449, RRID:AB_310624
Anti-rabbit 488 secondary antibody	Thermo Fisher SCIENTIFIC	A11034, RRID:AB_2576217
Anti-mouse 488 secondary antibody	Thermo Fisher SCIENTIFIC	A11001, RRID:AB_2534069
Anti-rabbit555 secondary antibody	Thermo Fisher SCIENTIFIC	A21429, RRID:AB_2535850
Anti-rat568 secondary antibody	Thermo Fisher SCIENTIFIC	A11077, RRID:AB_141874
Biological samples		
Mouse pre-implantation embryos	This paper	N/A
Chemicals, peptides, and recombinant proteins		
5-Iodo-2'-deoxyuridine (IdU)	Sigma-Aldrich	I7125
5-Chloro-2'-deoxyuridine (CldU)	Sigma-Aldrich	C6891
ERCC RNA Spike in Mix	Invitrogen	4456740
SuperScript III Reverse Transcriptase	Invitrogen	18080093
Proteinase K Solution (20 mg/mL), RNA grade	Thermo Fisher Scientific	25530049
Klenow fragment (3' to 5' exo-)	NEB	M0212
T4 DNA ligase	NEB	M0202
2x MyTaq red mix	Bioline	BIO-25043
Dpnl	NEB	R0176
NP-40 (10%)	Biovision	2111-100
3-Indoleacetic acid (Auxin)	Sigma Aldrich	I2886
Critical commercial assays		
10x Single Cell Lysis & Fragmentation Buffer	Sigma-Aldrich	L1043-500RXN
QIAquick 96-well purification kit	Qiagen	28181
NEBNext Ultra II DNA Library Prep Kit	NEB	E7645L
NEBNext Multiplex Oligos for Illumina	NEB	E6609S
SPRIselect	Beckman Coulter	B23318
Agilent High Sensitivity DNA Kit	Agilent	5067-4626
Clontech lysis buffer	Clontech	Z5013N
End-It DNA end-repair kit	Epicentre	ER81050
mMESSAGE mMACHINE T3 Transcription Kit	Invitrogen	AM1348
AMPure XP DNA magnetic beads	Beckman Coulter	A63881

(Continued on next page)

Continued

REAGENT or RESOURCE	SOURCE	IDENTIFIER
Deposited data		
scRepli-seq data	This paper	GSE262791
RNA-seq data	This paper	GSE262791
DamID-seq data	This paper	GSE262791
ATAC-seq data	Wu et al. ⁵²	GSE66581
H3K4me3 ChIP data	Zhang et al. ⁵³	GSE71434
H3K9me3 ChIP data	Wang et al. ⁵⁴	GSE98149
H3K27me3 ChIP data	Liu et al. ⁵⁵	GSE73952
DNAse-seq data	Wu et al. ⁵²	GSE135457
RNA-seq data	Deng et al. ⁴⁰	GSE45719
Hi-C compartment data	Du et al. ³⁰	GSE82185
Experimental models: Organisms/strains		
Mouse: C57BL/6J X CBA/H F1 mouse	Janvier labs, https://janvier-labs.com/ ; 22 Route des Chênes Secs, 53940 Le Genest-Saint-Isle, France	RRID:MGI:5650652
Mouse: DBA/2J mouse	Janvier labs, https://janvier-labs.com/ ; 22 Route des Chênes Secs, 53940 Le Genest-Saint-Isle, France	RRID:MGI:2684695
Oligonucleotides		
siGENOME Control siRNA	Dharmacon	D-001210-01-05
siGENOME siRNA Mouse Rif1	Dharmacon	D-040028-01-0005
Universal WGA primer	IDT	N/A
DamID Adapter_top: 5'-CTAATAC GACTCACTATAGGGCAGCGTGG TCGCGGCCGAGGA-3'	Sigma Aldrich	N/A
DamID Adapter_bottom: 5'-TCCTCGGCCGCG-3'	Sigma Aldrich	N/A
Barcoded DamID PCR primers: 5'-NNNNNNBARCODGTGGTCCG CGGCCGAGGATC-3'	Sigma Aldrich	N/A
Illumina sequencing adaptor mix and primers	Sigma Aldrich	N/A
Recombinant DNA		
pRN3P-AID-Dam-LaminB1	Borsos et al. ²⁸	N/A
pRN3P-TIR1-3XMyC	Borsos et al. ²⁸	Addgene #119766
pRN3P-EGFP-m6ATracer	Borsos et al. ²⁸	Addgene #139403
pRN3P-membrane-EGFP	Borsos et al. ²⁸	Addgene #139402
Software and algorithms		
Snakemake	Mölder et al. ⁵¹	https://snakemake.github.io
Bowtie2	Langmead and Salzberg ⁵⁶	https://bowtie-bio.sourceforge.net/bowtie2/index.shtml
Samtools	Danecek et al. ⁵⁷	https://www.htslib.org/doc/samtools.html
Picard	The Broad Institute, 320 Charles St, Cambridge, MA 02141, United States	https://broadinstitute.github.io/picard/
BEDTools	Quinlan and Hall ⁵⁸	https://bedtools.readthedocs.io/en/latest/
STAR	Dobin et al. ⁵⁹	https://github.com/alexdobin/STAR
R	R Core Team	https://www.r-project.org
Bioconductor	Huber et al. ⁶⁰	https://bioconductor.org
copynumber	Nilsen et al. ⁶¹	https://bioconductor.org/packages/3.16/bioc/html/copynumber.html

(Continued on next page)

Continued

REAGENT or RESOURCE	SOURCE	IDENTIFIER
mixtools	Benaglia ⁶²	https://cran.r-project.org/web/packages/mixtools/
Other		
Single-cell Repli-seq data processing pipeline	This study. https://doi.org/10.5281/zenodo.15038815	https://ascgitlab.helmholtz-muenchen.de/public_pipelines/repliseq_rif1
DamID data processing pipeline	Pal et al., in revision. https://doi.org/10.5281/zenodo.15038821	https://ascgitlab.helmholtz-muenchen.de/public_pipelines/damidseq_pipeline
Mouse reference genome GRCm38	ENSEMBL	http://ftp.ensembl.org/pub/release-101/fasta/mus_musculus/dna/Mus_musculus.GRCm38.dna.primary_assembly.fa.gz
Gene annotation	ENSEMBL	http://ftp.ensembl.org/pub/release-101/gtf/mus_musculus/Mus_musculus.GRCm38.101.gtf.gz
ERCC spike-in sequences and annotations	Thermo Fisher Scientific	https://assets.thermofisher.com/TFS-Assets/LSG/manuals/ERCC92.zip

EXPERIMENTAL MODEL AND STUDY PARTICIPANT DETAILS

Embryo collection and culture

All experimental work with animals are subjected to approval and were authorised the authorities from Upper Bavaria (Tierversuchsantrag von Regierung von Oberbayern) and follow the European and German legislation, which includes the RRR principle. Mice housed in Helmholtz Zentrum München were maintained and bred under institutional guidelines in a 12h light cycle at 20–24 °C and 45–65% humidity and constant access to food and water. F1 female mice (C57BL/6J × CBA) < 10 weeks of age were super-ovulated by intraperitoneal injection of 10 U of pregnant mare serum gonadotropin (PMSG) (Ceva) followed by 10 U of human chorionic gonadotropin (hCG) (MSD Animal Health) 48 hours later, and then mated with DBA/2J male mice. Zygotes were collected from the oviduct and cumulus cells were removed upon brief incubation in M2 media (Sigma, M7167) containing hyaluronidase (Sigma Aldrich, H4272). Zygotes were placed in drops of KSOM and cultured at 37 °C with 5% CO₂ until used for further experiments.

METHOD DETAILS

Immunostaining

Embryos injected with siRNA for control and *Rif1* at 17–18 hours post-hCG injection were cultured until they reached the 4-cell, 8-cell, morula, and blastocyst stages, and were collected at 52, 70, 90, and 92 hours post-hCG, respectively. Cells were washed with PBS, fixed for 15 min in 4% PFA in PBS at room temperature and permeabilised with 0.5% Triton X-100 in PBS for 15 min at room temperature. After three times washing with PBS, cells were blocked in 5% normal goat serum (Sigma, G9023) in PBS for 1 h at room temperature and incubated overnight at 4°C with the following primary antibodies: Rif1 UCR111 (1:1000 dilution), ¹⁴ γH2AX (ab2251, 1:1000 dilution), H3K4me3 (13-0041, 1:1000 dilution), H3K9me3 (ab8898, 1:500 dilution), H3K27me3 (07-449, 1:1000 dilution). After three times washing with PBS, the cells were incubated with the corresponding secondary antibodies (Anti-mouse Alexa 488; 1:800 dilution) (Anti-rabbit Alexa 488 or 555; 1:800 dilution). DNA was stained with 1 μg/ml 4',6-diamidino-2-phenylindole (DAPI). Images were acquired on a SP8 confocal laser-scanning microscope (Leica). We set acquisition parameters in order to obtain fluorescence intensity signal in the linear range of the hybrid detectors of the confocal microscope. These detectors have negligible detector noise and linearly amplify incoming photons into photoelectrons, thus enabling counting of measured photons as long as the detector is not saturated. The recovered signal therefore accurately reflects the level of antigen present in the system and quantifications are possible between experimental and control samples since, in addition, we used identical settings for acquisitions.

Quantification of RIF1 fluorescence intensity in 3D

We used an image analysis pipeline with the following software and software libraries (version numbers indicated): Fiji (ImageJ 1.54f),⁶³ Python (3.12.2), Cellpose (3.0.6),^{64,65} Pytorch (2.2.1), pytorch-cuda (11.8), cudnn (8.0), scikit-image (0.22),⁶⁶ pandas (2.2.1), R (4.3.1), and ggplot2 (3.4.3). First, we trained a custom Cellpose model using 66 single optical sections in the DAPI channel that were randomly extracted with Fiji for manual annotation. These images were split into a training and test dataset of which the latter contained 20% of all images. The Cellpose 'nuclei' model was then re-trained with these images and a mean object diameter of 75 pixels, as determined from the average size of training masks. The model was trained with default parameters, for 300 epochs. After manually checking the quality of several segmentation masks, we segmented the nuclei of mouse early 4-cell embryos and combined masks per optical section to obtain 3-dimensional volumes using a Cellpose 'stitch threshold' of 0.02. Finally, from the Cellpose masks and the raw intensity images, we extracted the mean intensity value for each cell in both DAPI and RIF1 channels

with the scikit-image 'regionprops' module. In 'R', we verified the distribution of volumes of the found objects and filtered out small objects (typically arising from segmentation of polar bodies or noisy regions in the DAPI channel). Plots were subsequently generated with ggplot2 and we performed statistical evaluation in 'R' with the Wilcoxon rank sum test.

DNA fibres

DNA fibres were prepared as described³² based on.⁶⁷ Embryos injected with siRNA for control and for *Rif1* at 17–18 hours post-hCG were cultured until they reached the morula stage and were sequentially pulse-labelled with 25 μ M IdU (Sigma, I7125) and 50 μ M CldU (Sigma, C6891) for 30 min each and collected at 89 hours post-hCG. Labelled embryos were lysed and DNA fibres were stretched onto the slide glass by tilting. The fibres were fixed in methanol/acetic acid (3:1), then denatured with 2.5 M HCl for 1 h, neutralised with PBS, and blocked with 1% BSA / 0.1% Tween 20 in PBS. CldU and IdU tracks were detected with anti-BrdU antibodies (described in [key resources table](#)) recognizing CldU and IdU, respectively, and appropriate secondary antibodies (described in [key resources table](#)). Images were acquired on a Leica SP8 confocal microscope using a 40x Plan/Apo NA1.3 oil immersion objective (Leica) at 2048x2048 pixels at an effective pixel size of 142 nm. To calculate fork speed, we used the established conversion 1 μ m = 2 kb.⁶⁸ Analysis of DNA fibres was performed as described before³² by two different researchers using a custom image analysis pipeline (<https://github.com/IES-HelmholtzZentrumMunchen/dna-fibres-analysis>) based in part on implementing a structure reconstruction with a spatially variant morphological closing.⁶⁹ We employed masks to select region of interest with sufficient amount of fibres and extracted fibres manually. To detect patterns in the extracted fibres, we used a branches detection strategy. Because the fluorescence channels are not directly comparable in absolute intensity values, we used the logarithm of their point-wise instead. We used regression trees structures in combination with the CART algorithm,⁷⁰ and a semi-automated step to verify fibre detection and assignment of patterns. To calculate inter-origin distance (IOD), we manually selected sufficiently long fibre stretches from the DNA fibre dataset in the DNA channel, which encompassed several IdU/CldU boundaries using a custom made Fiji (ImageJ) macro to open the regions of interest in the images and applied the ImageJ 'Straighten' function with a width of 19 pixels to convert bent fibres into approximately 2-dimensional images, where the channel intensities were interpolated along the x-axis. In the stretched fibre images, we then manually selected all identifiable IdU/CldU boundaries. The remaining analysis was performed in 'R'. We first calculated from the x-coordinates of the boundaries all origin positions by averaging between two adjacent boundary points. We then determined the pair-wise difference between origins to obtain the IOD. IOD and box plots were created with the ggplot2 library in 'R'.

Repli-seq

Single-cell Repli-seq in embryos was performed as we previously described¹⁰ based on references^{38,71}. Briefly, early stage zygotes were collected and micro-injected with 20 μ M siRNA at 17–18 hours post-hCG injection (phCG), and then they were cultured until they reached the S-phase at each developmental stage, based on their time after hCG injection. Embryos were collected at different time points at each developmental stage to achieve sampling over the entire S-phase. For each developmental stage, embryos were obtained from several litters and embryos from different litters were collected across different dates to ensure robust data collection. The number of mice and timing used to collect samples for each developmental stage are indicated in the parenthesis, respectively, as follows: siControl 4-cell (20, 50–56 hours post-hCG); siRIF1 4-cell (20, 50–56 hours post-hCG); siControl 8-cell (20, 65–71 hours post-hCG); siRIF1 8-cell (20, 65–71 hours post-hCG); siControl Morula (12, 90–96 hours post-hCG); siRIF1 Morula (12, 90–96 hours post-hCG). Zona pellucida was removed by exposure to acid Tyrode and each blastomere was dissociated by gentle pipetting after trypsin treatment. Individual blastomeres were placed into 8-strip PCR tubes containing lysis buffer (0.13mg/mL Proteinase K, 1x Single Cell Lysis & Fragmentation Buffer in H₂O) and extracted DNA was fragmented by heat incubation. Fragmented DNA was tagged by the universal WGA primer (5'-TGTGTTGGGTGTGTTTGGKKKKKKKKNN-3') and amplified with WGA primer sets which have individual barcode. Amplified DNA was purified by the QIAquick 96 PCR Purification Kit (QIAGEN, 28181) and concentration was determined by the NanoDrop (Thermo Scientific). Equal amount of DNA from each sample (up to 96 samples) were pooled and 1 μ g of them was ligated with the Illumina adaptors using the NEBNext Ultra II DNA Library Prep Kit (NEB, E7645L). Illumina sequences (NEBNext Multiplex Oligos for Illumina; NEB, E6609S) were added to the adaptor-ligated samples by PCR. Clean up and size selection of the PCR product was done using SPRIselect (Beckman Coulter, B23318) and the quality of the library was confirmed by 2100 Bioanalyzer with the High Sensitivity DNA Kit (Agilent, 5067-4626).

scRepli-seq read alignment and quality control filtering

The summary of sample collection, alignment statistics and data quality is included in [Table S1](#). Sequencing reads were mapped to the GRCh38 genome using bowtie2 (version 2.5.1)⁵⁶ with the parameters `-local -no-unal -no-mixed -no-discordant`. Reads were filtered by mapping quality using samtools with the parameter `-q 20`. Read duplicates were removed using picard MarkDuplicates (version 3.0.0) with the parameter `-REMOVE_DUPLICATES true`. Using bedtools intersect (version 2.31.0),⁵⁸ reads were counted in consecutive 50kb genomic bins. For each cell, the mean of the bin counts was calculated per chromosome to obtain the between chromosome coefficient of variation (CoV) as the ratio of the standard deviation to the mean ([Figure S1F](#)). Cells with a CoV threshold above 0.15 were filtered out from the analyses. The threshold was set to be able to process a large number of single cells and to accommodate the observed higher coefficient of variation in RIF1-depleted embryos. Cells were added back if the CoV threshold was not passed due to an individual chromosome, which was masked. The CoV filter serves to remove cells with abnormal, aneuploid genotypes. Finally, cells with more than 750,000 mapped reads were used for downstream analyses.

Assignment of replication status

Read counts in consecutive 50kb genomic bins were used in the scRepli-seq bioinformatic pipeline that we previously described.¹⁰ Briefly, bin counts were first RPM (reads per million) normalized. To correct for the mappability bias, for each bin its respective average of all samples within the same condition was calculated. Outlier regions (<5th percentile and >1st percentile) were masked. To correct for low mappability, bins were segmented with the R package *copynumber*⁶⁰ (version 1.38.0, R version 4.2.3)⁶¹ and segments with the highest 95% of values were kept. For each cell, the data were centered by the mean and scaled by the interquartile range and smoothed by a median filter (running window width of 15), followed by segmentation with the R package *copynumber*. The segmented values were used to fit a two component mixture model to identify replicated and non-replicated genomic bins using the R package *mixtools* (version 2.0.0).⁶² To find a threshold that separates the bins, the intersect of two normal distribution functions were used. If no intersect was found, the center of the means served as threshold, as previously described.¹⁰

Replication score, bin-bin distance, replication timing value and variability score

Genome-wide replication score was defined as the percentage of replicated genomic bins for each cell. Cells with a replication score greater than 90% and less 10% were removed from the analysis. We ranked the cells by the replication score as a proxy of S-phase progression for visualization on the binary replicated/non-replicated heatmaps (Figures 1E–1G). To assess the relationship between genomic regions we calculated the Manhattan distance between all pairs of genomic bins across cells on the binarized data ('1s' replicated, '0s' non-replicated). The distance matrix was centered by the mean and visualized as heatmap (Figures 1H–1J). Because the RT values are relative (maximum value is always 1 and minimum value is always 0) and the Manhattan distances are centered, the data between two experimental conditions are comparable. To obtain replication timing values and to correct for potential sampling bias of cells, we calculated the fraction of replicated cells in overlapping intervals of the genome-wide replication score with interval size of 35% and increment of 4.33% (e.g. 0–35%, 4.33–39.33% etc.) for each genomic bin. The average of these 16 intervals served as replication timing value that was used for downstream analyses. A higher replication timing value indicates earlier replication timing, as higher proportion of cells replicated the bin. The variability score was calculated as described elsewhere.¹⁰ For the PCA analysis, we used a given percentage of the most variable bins (i.e. to minimise noise and capture the most meaningful signal that reduces dimensionality). We display the data with the 25% most variable bins but we obtained similar trends using a higher number of bins.

Identification of IZs (RT peaks), TTRs and TZs (RT troughs)

IZs, TTRs and TZs were defined based on the replication timing values as described before.^{8,10} Briefly, genomic bins were grouped into 15 clusters by their replication timing values using the *Mclust* function from the *mclust* (version 6.0.0) R package (R version 4.1.2). The clusters were ranked by their average replication timing. IZs or TZs were defined as consecutive bins with local maxima or local minima of their cluster ranks, respectively, in sliding windows of 21 genomic bins using the *rollapply* function from *zoo* R package (version 1.8–10). Regions between IZs and TZs were defined as TTRs.

Analysis of RT heterogeneity

Heterogeneity analysis was performed using the sigmoidal model fitted for each genomic bin as described previously.^{10,38,61,62,72} Two parameters were calculated from the curve fitting, M-value and T_{width} . The M-value (sometimes also referred to as T_{rep} in the literature⁸) is the replication score (\sim S-phase time) at which 50% of the cells replicated the given bin. A greater M-value indicates later replication timing. T_{width} is a measure of RT heterogeneity and is defined as the replication score difference (\sim S-phase time difference) between 25% and 75% of the cells replicated the genomic bin. A higher T_{width} value indicates greater heterogeneity, as the transition from non-replicated to replicated status is larger.

scRepli-seq statistical analysis

For statistical analyses of scRepli-seq, we used a bootstrapping method and calculated 95% confidence intervals to determine statistical significance.⁷³ We have previously used this method¹⁰ as it avoids the inflation of p-values when n is large due to large number of genomic bins ($n \sim 49000$) and thus we applied bootstrapping to single cells ($n \sim 30-70$). Namely, we iteratively re-sampled individual cells with replacement 1000x times for each condition and calculated confidence intervals from the bootstrap distribution using the percentile method. The 95% percent confidence interval is the interval between 2.5th and 97.5th percentile of the distribution. When 95% percent confidence intervals do not include zero or two intervals do not overlap, they are significantly different from zero or different from each other, respectively. Using the bootstrap method, we called genomic bins that are significantly different between conditions (e.g. siRIF1 vs. siControl). We also applied the bootstrap method to judge the significance of the differences in the mean variability score (Figure S1I), the IQR of the M-values (Figure S2H), and the mean of T_{width} (Figure S2J).

Single embryo RNA-seq and library preparation

20 μ M siControl (Dharmacon, D-001210-01) or 20 μ M siRIF1 (Dharmacon, D-040028-01) were injected into zygotes at 17–18 hpgCG injection and embryos were cultured until 63 and 70 hours post-hCG injection, respectively, at which point 4-cell and 8-cell embryos, respectively were collected, washed with PBS, placed in tubes with 1 \times Clontech lysis buffer (Clontech, Z5013N) containing ERCC RNA Spike-In Mix (Invitrogen, 4456740) and flash-frozen in liquid nitrogen. The *Rif1* siRNA used in this study was previously validated against 3 other individual siRNAs.⁴⁷ RNA-seq was carried out using the SMART-seq2 protocol⁷⁴ and subjected to 150bp paired-end sequencing on a Novaseq 6000 (Illumina) platform. The quality and quantity of the cDNA libraries were verified with the 2100

Bioanalyzer with the High Sensitivity DNA Kit (Agilent, 5067-4626). A total of seven siControl and thirteen siRIF1 injected 4-cell embryos and eight siControl and twelve siRIF1 injected 8-cell embryos derived from two independent experiments were sequenced. Collection developmental timepoints for RNA-seq, which overlap with S-phase, were chosen to enable comparisons across public datasets but, most importantly, because most of the transcriptional changes occur during the course of S-phase due to the short duration of G1 in mouse embryos (only 1-2 hours).

RNA-seq analysis

Sequencing reads (paired) were aligned to the mouse genome (GRCm38, primary assembly) using STAR aligner (version 2.7.6a)⁵⁹ with the annotation (GRCm38.101) and ERCC92 (ThermoFisher). Reads were counted per gene by the same STAR run by setting `quantMode GeneCounts`. Downstream data analysis and visualization was done using R (version 4.1.2). Embryos with at least 500,000 genic reads, less than 20% ERCC and mitochondrial reads were considered. Differential expression analysis was performed with DESeq2 (version 1.34.0) and functions from `HelpersforDESeq2` package (link: <https://github.com/tschauer/HelpersforDESeq2>). Genes were filtered for at least one read counted in at least one fourth of all samples. Differentially expressed genes were called by a cut-off of an adjusted *p*-value of less than 0.05. Results were visualized as the relationship between the log₂ fold change of siRIF1 vs. siControl and the log₁₀ mean normalized counts on MA-plots.

DamID-sequencing and analysis

Zygotes were collected and injected with 20 μM siRNA at 17-18 hours post-hCG, followed by culture in KSOM medium until the late 2-cell stage. At 46-48 hours post-hCG, both blastomeres of the 2-cell embryos were injected with 250 ng/μL Tir1, 100 ng/μL membrane-eGFP, and 20 ng/μL AID-Dam-LaminB1 of in vitro transcribed mRNA, and subsequently cultured in medium containing auxin (Sigma, I2886, 500 μM). For DamID the 4-cell stage, auxin was removed at 54 hours post-hCG, and late 4-cell embryos were collected at 60-62 hours post-hCG. For DamID in the late 8-cell stage, auxin was washed out from 66 to 72-74 hours post-hCG. Before processing for DamID, the zona pellucida was removed by treatment with 0.5% pronase in M2 at 37 °C for 5 minutes and the polar body was removed by gentle pipetting after trypsin treatment. For each replicate, a pool of 16-24 blastomeres (four to six 4-cell embryos or two to three 8-cell embryos) was collected in 2 μL DamID buffer and stored at -80 °C until processing. All experiments were conducted in three independent biological replicates. Sample processing and library preparation were performed as previously described.^{28,75} Libraries were sequenced using Illumina HiSeq2500 platform in 150 bp PE mode but only the first read was used for analysis. The first 6 random bases of reads were discarded by `trimmomatic` (version 0.39) and reads were demultiplexed by the DamID indexes. The processed reads starting with GATC were then aligned to the GRCm38 using `bowtie2` (version 2.5.1) with default settings. Reads with a mapping quality score below 30 were removed using `samtools` (version 1.17).⁵⁷ Duplicated reads were filtered using `picard` (version 3.0.0). Reads were counted in 100kb consecutive genomic bins using `bedtools` (version 2.31.0).⁵⁸ OE (Observed/Expected) values per bin were calculated similarly as described previously.⁷⁶ Briefly, genomic GATC sites were extended to the trimmed read length (123 bp) in both directions using R (version 4.1.2) `Biostrings` (version 2.62.0) and `GenomicRanges` (version 1.46.1) packages.⁶⁰ GATC reads were processed the same way as DamID reads (observed) and served as expected reads counts. Read counts were normalized by rpkms (reads per kilobase per million) and the smallest non-zero rpkms value (pseudo-count) was added. The final DamID Score was calculated as the ratio of the observed over expected rpkms values. Bins with zero rpkms for both observed and expected values were treated as zero. OE mean signal was obtained by averaging the rpkms values of the biological replicates prior OE value calculation. The OE mean values were used for visualization and LAD calling. To distinguish between LADs and iLADs, a two-state hidden Markov model (HMM)⁷⁷ was used on the non-zero OE mean values. For differential analysis between siRIF1 and siControl at genomic bins, a generalized linear model of the gamma family with log link was fitted on the replicate OE values using R as described previously (Pal et al., in revision). *P*-values were obtained on the *z*-distribution and were corrected for multiple testing by the Benjamini & Hochberg procedure. Significant bins were identified by an adjusted *p*-value threshold of 0.01 and a log₂ fold change threshold of one.

Analysis of public chromatin datasets

Published datasets were obtained from GEO with accession numbers GSE66581 (ATAC-seq⁵²), GSE71434 (H3K4me3 ChIP⁵³), GSE98149 (H3K9me3 ChIP⁵⁴), GSE73952 (H3K27me3 ChIP⁵⁵) and GSE135457 (DNase-seq⁵²). Paired-end reads were trimmed by `cutadapt` (version 3.4) with parameters `-a CTGTCTCTTATA -A CTGTCTCTTATA -a AGATCGGAAGAGC -A AGATCGGAAGAGC -minimum-length=20`. After trimming, reads were mapped to the mouse reference (GRCm38) using `bowtie2` (version 2.3.5) with parameters `-end-to-end -very-sensitive -no-unal -no-mixed -no-discordant -I 10 -X 500`. Reads were filtered by mapping quality by `samtools` (version 1.3) with parameter `-q 12`. Read pairs were imported to R (version 4.1.2) using the `readGAlignmentPairs` function from the `GenomicAlignments` package (version 1.30.0)⁶⁰ and unique fragments were selected. Mitochondrial reads and reads mapped to scaffolds were not considered. Fragments were counted with the `countOverlaps` function from the `GenomicRanges` package (version 1.46.1) in 50kb consecutive genomic bins, normalized by the sum of the fragments counts and multiplied by a million. Normalized counts were log₂ transformed after adding a pseudo-count of 0.1.

Analysis of publicly available RNA-seq datasets

Published RNA-seq datasets were downloaded from GEO with accession number GSE45719.⁴⁰ Data processing, read counting and TPM calculations were carried out as described in.⁷⁸ Early blastocyst cells were further divided to ICM and TE cells by hierarchical

clustering on the TPM values of selected marker genes.⁷⁸ For direct comparison between RT, DamID OE values and RNA-seq, we counted the RNA-seq reads in 100kb consecutive bins similarly to ChIP-seq datasets as described above.

Analysis of public Hi-C dataset

Hi-C compartment coordinates and scores (GSE82185)³⁰ were analyzed as described.²⁸

Image analysis of morula and blastocyst stage embryos

For segmentation of cells in morula and blastocysts, we first manually outlined individual embryos in Fiji⁶³ then segmented cells of each embryo using the DAPI channel with Cellpose (version 3.0.6 and 2.0.5, respectively)^{64,65} using a custom-trained model, or the 'nuclei' model, respectively. In both cases, we used a radius of 80 pixels for object detection and a stitch threshold of 0.01 to assemble 2D segmentation masks into 3D objects. For analysis of phosphorylated H2A.X intensities we applied the 'regionprops' module of the 'scikit-image' Python package (version 0.22.0)⁶⁶ with the phosphorylated H2A.X channel as 'intensity_image' parameter. For detection of mitotic cells in blastocysts, we trained a pixel classifier in Ilastik (version 1.4.0)⁷⁹ on DAPI images. Mitotic cells were defined by applying hysteresis thresholding on the Ilastik probabilities (low threshold 0.5, high threshold 0.99) and further refined by removing small objects with volumes < 3000 voxels. The post-processed Ilastik masks were then counted to derive the number of mitotic cells per embryo or subtracted from Cellpose masks to quantify the number of interphase cells per embryo. Data were exported to csv files with the Python 'pandas' package. We only considered embryos with more than 9 cells. Data were plotted in 'R' (version 4.3.1) with the 'ggplot2' package (version 3.4.3). Statistical tests were performed by Wilcoxon rank sum exact test, or a generalized linear model with 'poisson' parameter for evaluating count data.

QUANTIFICATION AND STATISTICAL ANALYSIS

Details on all statistical analyses used are described in the corresponding Figure Legends. An expanded description of statistical analyses is further included in the corresponding sections in the [STAR Methods](#) for completeness. Across all experiments, n indicates the number of embryos analysed and N the number of independent experiments, which is indicated in the Figure Legends. All the features for the plots are fully described in the Figure Legends. No methods were used to determine whether the data met assumptions for statistical analysis.